Accepted Manuscript

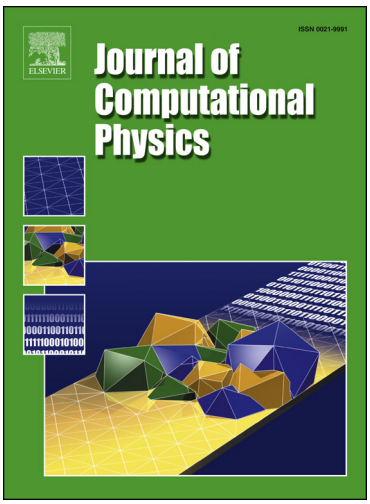

High-order shock-fitted detonation propagation in high explosives

Christopher M. Romick, Tariq D. Aslam

PII: S0021-9991(16)30641-6
DOI: http://dx.doi.org/10.1016/j.jcp.2016.11.049
Reference: YJCPH 6999

To appear in: *Journal of Computational Physics*

Received date: 11 October 2016
Revised date: 29 November 2016
Accepted date: 30 November 2016

Please cite this article in press as: C.M. Romick, T.D. Aslam, High-order shock-fitted detonation propagation in high explosives, *J. Comput. Phys.* (2016), http://dx.doi.org/10.1016/j.jcp.2016.11.049

Highlights

- A highly accurate shock fitting scheme for high explosive simulations is developed.
- The method restores the possibility of high-order rates of convergence.
- The method offers an approach to improve the calibration of HE models.

High-Order Shock-Fitted Detonation Propagation in High Explosives

Christopher M. Romick[1], Tariq D. Aslam[2]

Abstract

A highly accurate numerical shock and material interface fitting scheme composed of fifth-order spatial and third- or fifth-order temporal discretizations is applied to the two-dimensional reactive Euler equations in both slab and axisymmetric geometries. High rates of convergence are not typically possible with shock-capturing methods as the Taylor series analysis breaks down in the vicinity of discontinuities. Furthermore, for typical high explosive (HE) simulations, the effects of material interfaces at the charge boundary can also cause significant computational errors. Fitting a computational boundary to both the shock front and material interface (*i.e.* streamline) alleviates the computational errors associated with captured shocks and thus opens up the possibility of high rates of convergence for multi-dimensional shock and detonation flows. Several verification tests, including a Sedov blast wave, a Zel'dovich-von Neumann-Döring (ZND) detonation wave, and Taylor-Maccoll supersonic flow over a cone, are utilized to demonstrate high rates of convergence to nontrivial shock and reaction flows. Comparisons to previously published shock-capturing multi-dimensional detonations in a polytropic fluid with a constant adiabatic exponent (PF-CAE) are made, demonstrating significantly lower computational error for the present shock and material interface fitting method. For an error on the order of 10 m/s, which is similar to that observed in experiments, shock-fitting offers a computational savings on the order of 1000. In addition, the behavior of the detonation phase speed is examined for several slab widths to evaluate the detonation performance of PBX 9501 while utilizing the Wescott-Stewart-Davis (WSD) model, which is commonly used in HE modeling. It is found

[1]Eureka Physics LLC, Washington, DC 20002.

[2]Explosive Science and Shock Physics Division, Shock and Detonation Physics Group (M-9), Los Alamos National Laboratory, Los Alamos, New Mexico 87545, USA

that the thickness effect curve resulting from this equation of state and reaction model using published values is dramatically more steep than observed in recent experiments. Utilizing the present fitting strategy, in conjunction with a nonlinear optimizer, a new set of reaction rate parameters improves the correlation of the model to experimental results. Finally, this new model is tested against two dimensional slabs as a validation test.

Keywords: Numerical methods, Shock-fitting, Detonation, High Explosives

1. Introduction

Insensitive high explosives (IHE), like PBX 9502, have many benefits such as improved safety characteristics[1]; however, these IHEs exhibit longer reaction zones than more conventional high explosives (CHE). This makes IHEs less ideal explosives and thus more susceptible to edge effects. These effects can lead to considerable performance degradation, including the detonation speed being affected in large regions. It has been shown that in order to obtain $\mathcal{O}(50\ m/s)$ error in the steady, propagating detonation speed using an essentially non-oscillatory (ENO) in combination with Lax-Friedrichs (LF) shock-capturing that a minimum of 50 points were needed in the reaction zone [2]. This becomes prohibitively more computationally intensive as the requested error on the detonation velocity is reduced to typical experimental uncertainties of $\mathcal{O}(10\ m/s)$.

In addition, many constructions used in reactive high explosive (HE) modeling *e.g.* WSD[3], SURF[4], CREST[5], employ the shock state or related to this, the entropy of the reactants, in the reaction rates. In the common practice of shock-capturing, the inherent numerical viscosity smooths the shock at the expense of thickening its width. This, of course, introduces some ambiguity into what is the actual shock state. In order to remove this ambiguity, shock-fitting can be utilized. In this methodology, the shock front becomes one of the computational boundaries. Moreover, this restores the potential for highly accurate solutions for flows with a discontinuity as it effectively separates the ambient upstream and smooth reactive flow behind the front.

This potential has been demonstrated for non-reacting flows over blunt bodies in ideal gases [6]. In fact, even spectral methods have been developed for these flows, including those of an axisymmetric nature, by [7, 8, 9]. Moreover, shock-fitting has been successfully applied to produce highly accurate

solutions for one-dimensional pulsating detonations by [10]. The objective of this paper is to present a shock and material interface fitting method that can be applied to two-dimensional detonations in either slab or asymmetric geometries to provide highly accurate predictions.

The remainder of the paper is laid out as follows. First, the governing equations are outlined along with associated boundary conditions. Next, the computational algorithm is outlined starting with the transformation of Euclidean space-time to the computational shock and material interface domain. This transformation is also accompanied by the numerical scheme, which is presented with special care near the edges of the computational domain. Then, several verification examples are given, including a Sedov blast wave, a ZND detonation wave, and Taylor-Maccoll supersonic flow past a cone. This is followed by a comparison between shock-capturing and the presented fitting strategy in a slab geometry utilizing a mixture of polytropic fluids with a constant adiabatic exponent previously explored by [2]. The required resolution for a specified error-tolerance on the steady phase speed of the detonation is much less for the shock-fitting method than for capturing. Next, the fitting algorithm is used to evaluate detonation performance using a more realistic reactive flow model of PBX 9501 in a slab geometry. It is found that the predicted thickness effect curve, produced utilizing the published values of [11] for this model, is steeper than that observed in experiments. In addition, the present method is also used to predict the corresponding diameter effect curve for PBX 9501. A re-calibrated set of WSD parameters is determined for detonation propagation of PBX 9501 via nonlinear optimization of rate parameters, demonstrating the utility of the new method. Finally, this calibrated model is utilized to produce a thickness effect curve as a validation test.

2. Governing Equations

This work is focused on detonation propagation in a non-diffusive fluid in the absence of body forces. As such the governing equations are the unsteady, compressible, reactive Euler equations. Furthermore, this paper will be restricted to models of a single reaction, where the reactant, $\mathcal{R}$, goes irreversibly to product, $\mathcal{P}$ ($\mathcal{R} \rightarrow \mathcal{P}$). These equations can be written in conservative form in Gibbs notation as

$$\frac{\partial \rho}{\partial t} + \boldsymbol{\nabla \cdot} (\rho \boldsymbol{u}) = 0, \tag{1}$$

$$\frac{\partial}{\partial t}\left(\rho \mathbf{u}\right) + \boldsymbol{\nabla}\boldsymbol{\cdot}\left(\rho \boldsymbol{u}\boldsymbol{u}\right) + \boldsymbol{\nabla} p = 0, \tag{2}$$

$$\frac{\partial}{\partial t}\left(\rho e_t\right) + \boldsymbol{\nabla}\boldsymbol{\cdot}\left(\boldsymbol{u}\left(\rho e_t + p\right)\right) = 0, \tag{3}$$

$$\frac{\partial}{\partial t}\left(\rho \lambda\right) + \boldsymbol{\nabla}\boldsymbol{\cdot}\left(\rho \lambda \boldsymbol{u}\right) = \rho R, \tag{4}$$

where, t is the temporal coordinate, ρ the density, $\boldsymbol{u}$ the velocity vector, p the pressure, $E = \rho e_t$ the total energy, e_t the specific total energy which is composed of both internal energy and kinetic energy $\left(e_t \equiv e + \frac{\boldsymbol{u}\boldsymbol{\cdot}\boldsymbol{u}}{2}\right)$, e the specific internal energy, $\frac{\boldsymbol{u}\boldsymbol{\cdot}\boldsymbol{u}}{2}$ the specific kinetic energy, λ the reaction progress variable, R the reaction rate and ∇ the spatial gradient operator. The reaction progress variable is related to the mass fractions of the two species by $Y_{\mathcal{R}} = 1 - \lambda$ and $Y_{\mathcal{P}} = \lambda$. Equations 1-3 are expressions of the conservation of mass, linear momenta, and energy. The evolution of the reaction progress is described by Eqn. 4.

These equations must be further supplemented by constitutive relations for the equation of state (EOS) for the HE, $e\left(\rho, p, \lambda\right)$, as well as the reaction rate, R. Two separate equations of state will be examined in this work : 1) a mixture of polytropic fluids with a constant adiabatic exponent (PF-CAE) and 2) the Wescott-Stewart-Davis (WSD) model [3]. Most of this work will utilize the PF-CAE EOS and is simply detailed as

$$e = \frac{p}{\left(\gamma - 1\right)\rho} - \lambda q, \tag{5}$$

where γ is the adiabatic exponent and q the heat release of the reaction. This equivalent to the EOS of a calorically perfect mixture of ideal gases for $1 \leq \gamma \leq 5/3$. The WSD EOS model is detailed by [3] and [11]. The reaction rate model in [11] is given by

$$R = a\left(1 - \lambda\right)^{\nu}\left(\frac{p}{B}\right)^{N_p}\exp\left(\frac{-\rho E}{p}\right), \tag{6}$$

where a is the reaction rate constant, ν the depletion exponent, B the pressure scaling factor, N_p the pressure dependence exponent, and E the activation energy. The pressure scaling factor for the PF-CAE EOS is usually 1 and for the WSD EOS, it is the Chapman-Jouguet (CJ) (fully-reacted) pressure $\left(p_{CJ}\right)$.

2.1. Two-Dimensional Cartesian

For a slab orientation as shown in Fig. 1 with infinite depth in the $y-$direction, Eqns. 1-4 can be expanded as

$$\frac{\partial \rho}{\partial t} + \frac{\partial}{\partial x}\left(\rho u_x\right) + \frac{\partial}{\partial z}\left(\rho u_z\right) = 0, \tag{7}$$

$$\frac{\partial}{\partial t}\left(\rho u_x\right) + \frac{\partial}{\partial x}\left(\rho u_x u_x + p\right) + \frac{\partial}{\partial z}\left(\rho u_x u_z\right) = 0, \tag{8}$$

$$\frac{\partial}{\partial t}\left(\rho u_z\right) + \frac{\partial}{\partial x}\left(\rho u_z u_x\right) + \frac{\partial}{\partial z}\left(\rho u_z u_z + p\right) = 0, \tag{9}$$

$$\frac{\partial}{\partial t}\left(\rho e_t\right) + \frac{\partial}{\partial x}\left(\left(\rho e_t + p\right) u_x\right) + \frac{\partial}{\partial z}\left(\left(\rho e_t + p\right) u_z\right) = 0, \tag{10}$$

$$\frac{\partial}{\partial t}\left(\rho \lambda\right) + \frac{\partial}{\partial x}\left(\rho \lambda u_x\right) + \frac{\partial}{\partial z}\left(\rho \lambda u_z\right) = \rho R. \tag{11}$$

Here, u_x and u_z are the x and z direction components of the velocity vector, respectively.

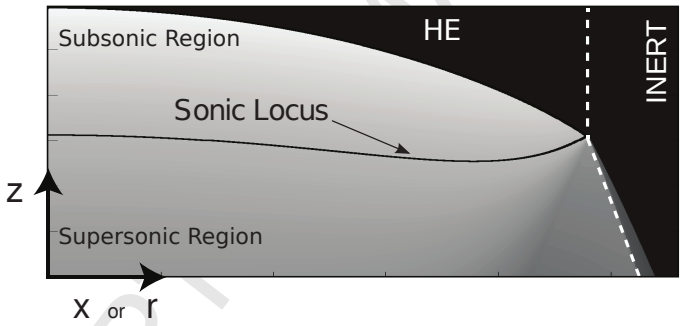

Figure 1
Two-dimensional geometry (slab or axisymmetric rate-stick) with the detonation traveling upwards and $x = 0$ or $r = 0$ marking the plane of symmetry. The black curve denotes the sonic locus in the HE; the white dashed line denotes the HE and inert confiner interface.

2.2. Axisymmetric Cylindrical

For axisymmetric cylinders of a HE, also known as rate-sticks, the state variables can be independent of azimuthal angle, θ in the three-dimensional (r, θ, z) coordinate system. Using this assumption for a rate-stick orientation as shown in Fig. 1, Eqns. 1-4 can be expanded as

$$\frac{\partial \rho}{\partial t} + \frac{1}{r}\frac{\partial}{\partial r}\left(r \rho u_r\right) + \frac{\partial}{\partial z}\left(\rho u_z\right) = 0, \tag{12}$$

$$\frac{\partial}{\partial t}\left(\rho u_r\right) + \frac{1}{r}\frac{\partial}{\partial r}\left(r\rho u_r u_r + p\right) + \frac{\partial}{\partial z}\left(\rho u_r u_z\right) = 0, \tag{13}$$

$$\frac{\partial}{\partial t}\left(\rho u_z\right) + \frac{1}{r}\frac{\partial}{\partial r}\left(r\rho u_z u_r\right) + \frac{\partial}{\partial z}\left(\rho u_z u_z + p\right) = 0, \tag{14}$$

$$\frac{\partial}{\partial t}\left(\rho e_t\right) + \frac{1}{r}\frac{\partial}{\partial r}\left(r\left(\rho e_t + p\right) u_r\right) + \frac{\partial}{\partial z}\left(\left(\rho e_t + p\right) u_z\right) = 0, \tag{15}$$

$$\frac{\partial}{\partial t}\left(\rho\lambda\right) + \frac{1}{r}\frac{\partial}{\partial r}\left(r\rho\lambda u_r\right) + \frac{\partial}{\partial z}\left(\rho\lambda u_z\right) = \rho R. \tag{16}$$

Here, u_r and u_z are the r and z direction components of the velocity vector, respectively. By expanding the r direction derivatives in Eqns. 12-16, the axisymmetric cylindrical equations can be written as

$$\frac{\partial \rho}{\partial t} + \frac{\partial}{\partial r}\left(\rho u_r\right) + \frac{\partial}{\partial z}\left(\rho u_z\right) = \frac{-\rho u_r}{r}, \tag{17}$$

$$\frac{\partial}{\partial t}\left(\rho u_r\right) + \frac{\partial}{\partial r}\left(\rho u_r u_r + p\right) + \frac{\partial}{\partial z}\left(\rho u_r u_z\right) = \frac{-\rho u_r u_r}{r}, \tag{18}$$

$$\frac{\partial}{\partial t}\left(\rho u_z\right) + \frac{\partial}{\partial r}\left(\rho u_z u_r\right) + \frac{\partial}{\partial z}\left(\rho u_z u_z + p\right) = \frac{-\rho u_r u_z}{r}, \tag{19}$$

$$\frac{\partial}{\partial t}\left(\rho e_t\right) + \frac{\partial}{\partial r}\left(\left(\rho e_t + p\right) u_r\right) + \frac{\partial}{\partial z}\left(\left(\rho e_t + p\right) u_z\right) = \frac{-\left(\rho e_t + p\right) u_r}{r}, \tag{20}$$

$$\frac{\partial}{\partial t}\left(\rho\lambda\right) + \frac{\partial}{\partial r}\left(\rho\lambda u_r\right) + \frac{\partial}{\partial z}\left(\rho\lambda u_z\right) = \rho R - \frac{\rho\lambda u_r}{r}. \tag{21}$$

This approach allows the same variables to be evolved in the both the Cartesian and axisymmetric cases. An alternative approach could be to account for the effects of this different geometry in a stronger conservative form [12]. However, the later approach leads to a different set of the evolved variables in the axisymmetric case versus the Cartesian case.

2.3. General Form

Equations 17-21 are in a similar form to those for the two-dimensional Cartesian slab geometry (Eqns. 7-11) with added source terms due to the axisymmetric nature of the rate-stick. Furthermore, these equations can be written in the form of

$$\frac{\partial \boldsymbol{U}}{\partial t} + \frac{\partial}{\partial \chi}\left(\boldsymbol{f}_\chi\left(\boldsymbol{U}\right)\right) + \frac{\partial}{\partial z}\left(\boldsymbol{f}_z\left(\boldsymbol{U}\right)\right) = \boldsymbol{S}\left(\boldsymbol{U}\right), \tag{22}$$

where the χ direction corresponds to the x or r direction depending on the nature of the geometry, *i.e.* slab or axisymmetric rate-stick, respectively.

The respective evolved state variables, $\boldsymbol{U}$, are

$$\boldsymbol{U} = \begin{cases} [\rho, \rho u_x, \rho u_z, \rho e_t, \rho\lambda]^T & \text{if slab,} \\ [\rho, \rho u_r, \rho u_z, \rho e_t, \rho\lambda]^T & \text{if axisymmetric,} \end{cases} \tag{23}$$

the respective χ direction fluxes are

$$\boldsymbol{f}_\chi = \begin{cases} [\rho u_x, \rho u_x u_x + p, \rho u_z u_x, (\rho e_t + p)\, u_x, \rho\lambda u_x]^T & \text{if slab,} \\ [\rho u_r, \rho u_r u_r + p, \rho u_z u_r, (\rho e_t + p)\, u_r, \rho\lambda u_r]^T & \text{if axisymmetric,} \end{cases} \tag{24}$$

the respective z direction fluxes are

$$\boldsymbol{f}_z = \begin{cases} [\rho u_z, \rho u_x u_z, \rho u_z u_z + p, (\rho e_t + p)\, u_z, \rho\lambda u_z]^T & \text{if slab,} \\ [\rho u_z, \rho u_r u_z, \rho u_z u_z + p, (\rho e_t + p)\, u_z, \rho\lambda u_z]^T & \text{if axisymmetric,} \end{cases} \tag{25}$$

and the respective source terms are

$$\boldsymbol{S} = \begin{cases} [0, 0, 0, 0, \rho R]^T & \text{if slab,} \\ \left[\frac{-\rho u_r}{r}, \frac{-\rho u_r u_r}{r}, \frac{-\rho u_r u_z}{r}, \frac{-(\rho e_t + p) u_r}{r}, \rho R - \frac{\rho\lambda u_r}{r}\right]^T & \text{if axisymmetric,} \end{cases} \tag{26}$$

where ^{T} indicates the transpose.

2.4. Boundary Conditions

Equation 22 needs to be supplemented by necessary physical boundary conditions. The first physical boundary location is the shock front at which the Rankine-Hugoniot jump conditions are applied. At the material interfaces and along symmetric boundaries, the velocity must be parallel to the interface. Lastly, in the supersonic portion of the flow beyond the sonic locus, the detonation products relax to a near-constant state relative to the large gradients observed in the reaction zone.

3. Numerical Implementation

In this section, the numerical algorithm for the multi-dimensional, high-order, shock-fitted method with deflected material interfaces is presented, and it is a natural extension of the work of [13] which was utilized in [14] with periodic boundary conditions. This numerical algorithm employs a method of lines approach. This supports separate spatial and temporal discretizations as well as allows the inclusion of source terms. In the following sections, the computational grid is defined, the spatial discretization is laid out, and the Runge-Kutta (RK) temporal scheme is detailed.

3.1. Transformed Grid

A frame of reference which is attached to the shock front is utilized for ease of computation of the detonation propagation. Behind the shock front, the reactant is converted to product releasing the stored chemical energy of the HE which drives the detonation forward. The products deflect the material interface outwards. This in turn slows the normal detonation speed near the material interface and gives rise to curvature of the front. Thus, both the shock front and material interfaces will need to be fit in order to maintain a highly-accurate solution.

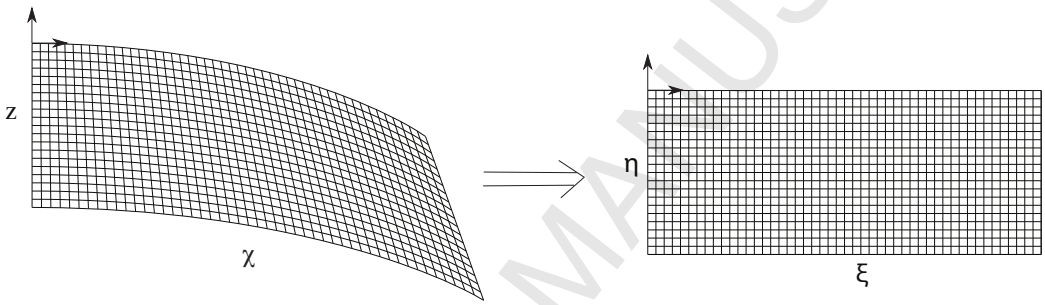

Figure 2
Demonstration of the transformation from the slab geometry to the computational domain. The detonation traveling upwards in the z-direction and $\chi = 0$ marks the plane of symmetry.

Here, the physical domain in the HE, which is assumed to be deformed by the passing detonation, will be transformed to a simple rectangular reference frame facilitating easy derivative flux calculations as shown Fig. 2. The transformation utilized in this work is

$$\chi\left(\xi,\eta,\tau\right) = \chi_l\left(\eta,\tau\right)\frac{\xi_r - \xi}{\xi_r - \xi_l} + \chi_r\left(\eta,\tau\right)\frac{\xi - \xi_l}{\xi_r - \xi_l}, \tag{27}$$

$$z\left(\xi,\eta,\tau\right) = z_s\left(\xi,\tau\right) + \eta, \tag{28}$$

$$t = \tau, \tag{29}$$

where $\chi_l\left(\eta,\tau\right), \chi_r\left(\eta,\tau\right)$ are the left and right physical boundaries, $z_s\left(\xi,\tau\right)$ defines the shock locus, and $\xi_l \equiv \chi_l\left(0,0\right), \xi_r \equiv \chi_r\left(0,0\right)$ the left and right transformed boundaries, respectively. This transformed domain consists of the ranges : $\xi_l \leq \xi \leq \xi_r$ and $0 \leq \eta \leq -\eta_{max}$. The transformation relates z and η linearly, offsetting the two by the position of the shock, z_s. In addition,

it uniformly distributes the χ positional coordinates along lines of constant η.

In this transformed frame, the governing equations (Eqn. 22) can be expanded using the chain rule as

$$\frac{\partial \boldsymbol{U}}{\partial \tau}\frac{\partial \tau}{\partial t}+\frac{\partial \boldsymbol{U}}{\partial \xi}\frac{\partial \xi}{\partial t}+\frac{\partial \boldsymbol{U}}{\partial \eta}\frac{\partial \eta}{\partial t}+\frac{\partial \boldsymbol{f}_\chi}{\partial \xi}\frac{\partial \xi}{\partial \chi}+\frac{\partial \boldsymbol{f}_\chi}{\partial \eta}\frac{\partial \eta}{\partial \chi}+\frac{\partial \boldsymbol{f}_z}{\partial \xi}\frac{\partial \xi}{\partial z}+\frac{\partial \boldsymbol{f}_z}{\partial \eta}\frac{\partial \eta}{\partial z}=\boldsymbol{S}. \quad (30)$$

Now, multiplying Eqn. 30 by the determinant of the metric tensor of the shock-fitted transformation, $\sqrt{g}=\frac{\partial \chi}{\partial \xi}\frac{\partial z}{\partial \eta}-\frac{\partial \chi}{\partial \eta}\frac{\partial z}{\partial \xi}$, and using the product rule to rearrange terms yields

$$\begin{aligned}
&\frac{\partial}{\partial \tau}\left(\sqrt{g}\boldsymbol{U}\right)+\frac{\partial}{\partial \xi}\left(\sqrt{g}\boldsymbol{U}\frac{\partial \xi}{\partial t}+\sqrt{g}\boldsymbol{f}_\chi\frac{\partial \xi}{\partial \chi}+\sqrt{g}\boldsymbol{f}_z\frac{\partial \xi}{\partial z}\right)\\
&\quad+\frac{\partial}{\partial \eta}\left(\sqrt{g}\boldsymbol{U}\frac{\partial \eta}{\partial t}+\sqrt{g}\boldsymbol{f}_\chi\frac{\partial \eta}{\partial \chi}+\sqrt{g}\boldsymbol{f}_z\frac{\partial \eta}{\partial z}\right)\\
&\quad-\boldsymbol{U}\left(\frac{\partial}{\partial \tau}\left(\sqrt{g}\right)+\frac{\partial}{\partial \xi}\left(\sqrt{g}\frac{\partial \xi}{\partial t}\right)+\frac{\partial}{\partial \eta}\left(\sqrt{g}\frac{\partial \eta}{\partial t}\right)\right)\\
&\quad-\boldsymbol{f}_\chi\left[\frac{\partial}{\partial \xi}\left(\sqrt{g}\frac{\partial \xi}{\partial \chi}\right)+\frac{\partial}{\partial \eta}\left(\sqrt{g}\frac{\partial \eta}{\partial \chi}\right)\right]\\
&\quad-\boldsymbol{f}_z\left[\frac{\partial}{\partial \xi}\left(\sqrt{g}\frac{\partial \xi}{\partial z}\right)+\frac{\partial}{\partial \eta}\left(\sqrt{g}\frac{\partial \eta}{\partial z}\right)\right]=\sqrt{g}\boldsymbol{S}. \quad (31)
\end{aligned}$$

Equation 31 can be further simplified using derivatives of the transformation Jacobian $\left(J=1/\sqrt{g}\right)$, which are developed in Appendix A. Using these derivatives, it can be shown that terms multiplied by leading $\boldsymbol{U}$, $\boldsymbol{f}_\chi$, and $\boldsymbol{f}_z$ terms are identically zero and thus, yielding

$$\begin{aligned}
&\frac{\partial}{\partial \tau}\left(\sqrt{g}\boldsymbol{U}\right)+\frac{\partial}{\partial \xi}\left(\sqrt{g}\boldsymbol{U}\frac{\partial \xi}{\partial t}+\sqrt{g}\boldsymbol{f}_\chi\frac{\partial \xi}{\partial \chi}+\sqrt{g}\boldsymbol{f}_z\frac{\partial \xi}{\partial z}\right)\\
&\quad+\frac{\partial}{\partial \eta}\left(\sqrt{g}\boldsymbol{U}\frac{\partial \eta}{\partial t}+\sqrt{g}\boldsymbol{f}_\chi\frac{\partial \eta}{\partial \chi}+\sqrt{g}\boldsymbol{f}_z\frac{\partial \eta}{\partial z}\right)=\sqrt{g}\boldsymbol{S}. \quad (32)
\end{aligned}$$

Moreover, using the spatial and temporal metric relationships,

$$\begin{aligned}
&\sqrt{g}\frac{\partial \xi}{\partial \chi}=\frac{\partial z}{\partial \eta},\quad \sqrt{g}\frac{\partial \xi}{\partial z}=-\frac{\partial \chi}{\partial \eta},\quad \sqrt{g}\frac{\partial \eta}{\partial z}=\frac{\partial \chi}{\partial \xi},\quad \sqrt{g}\frac{\partial \eta}{\partial \chi}=-\frac{\partial z}{\partial \xi},\\
&\sqrt{g}\frac{\partial \xi}{\partial t}=\left(\frac{\partial \chi}{\partial \eta}\frac{\partial z}{\partial \tau}-\frac{\partial z}{\partial \eta}\frac{\partial \chi}{\partial \tau}\right),\quad \sqrt{g}\frac{\partial \eta}{\partial t}=\left(\frac{\partial z}{\partial \xi}\frac{\partial \chi}{\partial \tau}-\frac{\partial \chi}{\partial \xi}\frac{\partial z}{\partial \tau}\right), \quad (33)
\end{aligned}$$

Eqn. 32 can be written in a very simple form

$$\frac{\partial}{\partial\tau}\left(\sqrt{g}\boldsymbol{U}\right)+\frac{\partial}{\partial\xi}\left(\frac{\partial z}{\partial\eta}\left(\boldsymbol{f}_{\chi}-\boldsymbol{U}\frac{\partial\chi}{\partial\tau}\right)-\frac{\partial\chi}{\partial\eta}\left(\boldsymbol{f}_{z}-\boldsymbol{U}\frac{\partial z}{\partial\tau}\right)\right)+\frac{\partial}{\partial\eta}\left(-\frac{\partial z}{\partial\xi}\left(\boldsymbol{f}_{\chi}-\boldsymbol{U}\frac{\partial\chi}{\partial\tau}\right)+\frac{\partial\chi}{\partial\xi}\left(\boldsymbol{f}_{z}-\boldsymbol{U}\frac{\partial z}{\partial\tau}\right)\right)=\sqrt{g}\boldsymbol{S}. \tag{34}$$

Here, there is a new set of conserved quantities, $\sqrt{g}\boldsymbol{U}$. In addition, the Cartesian fluxes of the conserved quantities, $\boldsymbol{U}$, relative to the moving frame are clearly recognizable. Moreover, the conserved momenta quantities result from the laboratory frame velocities, u_x or u_r and u_z, and not shock-attached frame velocities.

3.2. Shock Locus

In order to reduce the complexity in the current development of the algorithm, the material interfaces, χ_l and χ_r, will follow a prescribed motion in this paper. The prescribed motion reduces the unknown metrics of the transformation to $\partial z_s/\partial\tau$ and $\partial z_s/\partial\xi$. In a later paper, the development of the fitting procedure with a more general material interface motion will be presented. Therefore, the only remaining surface that must be fit in the current transformation is the shock locus. This corresponds to a coordinate curve in the shock conforming transformed space.

Based on the chosen transformation, the shock locus can be described as a level curve, such that

$$\eta\left(\chi,z,t\right)=0. \tag{35}$$

The rate of change of such a curve can be expanded using the chain rule as

$$\left.\frac{\partial\eta}{\partial\tau}\right|_{shock}=\left.\left(\frac{\partial\eta}{\partial t}\frac{\partial t}{\partial\tau}\right)\right|_{shock}+\left.\left(\frac{\partial\eta}{\partial\chi}\frac{\partial\chi}{\partial\tau}\right)\right|_{shock}+\left.\left(\frac{\partial\eta}{\partial z}\frac{\partial z}{\partial\tau}\right)\right|_{shock}=0. \tag{36}$$

Here, it can be seen that the time rate of change of the shock locus is the dot product of the gradient of the curve and the shock velocity. However, the motion of the shock still needs to be related to the flow. The discontinuity caused by the shock and its motion must be constrained by a balance of the fluxes of the conserved quantities with the surface forces across the shock. Therefore, by making such a substitution, Eqn. 36 can be rewritten as

$$\left.\frac{\partial\eta}{\partial t}\right|_{shock}=-\left.\left[\frac{\partial\eta}{\partial\chi}\frac{[\![\boldsymbol{f}_{\chi}]\!]}{[\![\boldsymbol{U}]\!]}+\frac{\partial\eta}{\partial z}\frac{[\![\boldsymbol{f}_{z}]\!]}{[\![\boldsymbol{U}]\!]}\right]\right|_{shock}. \tag{37}$$

Assuming that the shock locus is a smooth, continuous curve and utilizing the spatial metric relations from Eqns. 33 yields

$$\left.\frac{\partial \eta}{\partial t}\right|_{shock} = -\left[\frac{1}{\sqrt{g}}\frac{[\![-\boldsymbol{f}_\chi \frac{\partial z}{\partial \xi} + \boldsymbol{f}_z \frac{\partial \chi}{\partial \xi}]\!]}{[\![\boldsymbol{U}]\!]}\right]\Bigg|_{shock}. \tag{38}$$

Substituting the transformation of $\partial\eta/\partial t$ from Eqns. 33 into Eqn. 38 and rearranging terms gives the rate of change of the shock locus as

$$\frac{\partial z_s}{\partial \tau} = \left(\left(\frac{\partial \chi}{\partial \xi}\right)^{-1}\left[\frac{[\![-\boldsymbol{f}_\chi \frac{\partial z}{\partial \xi} + \boldsymbol{f}_z \frac{\partial \chi}{\partial \xi}]\!]}{[\![\boldsymbol{U}]\!]} + \frac{\partial z}{\partial \xi}\frac{\partial \chi}{\partial \tau}\right]\right)\Bigg|_{shock}, \tag{39}$$

where again z_s is the shock locus.

In addition, an evolution equation is needed for the one remaining unknown metric, $\partial z_s/\partial \xi$. This evolution of the shock slope can be obtained by differentiating Eqn. 39 with respect to ξ :

$$\frac{\partial}{\partial \tau}\left(\frac{\partial z_s}{\partial \xi}\right) = \frac{\partial}{\partial \xi}\left(\left(\frac{\partial \chi}{\partial \xi}\right)^{-1}\left[\frac{[\![-\boldsymbol{f}_\chi \frac{\partial z}{\partial \xi} + \boldsymbol{f}_z \frac{\partial \chi}{\partial \xi}]\!]}{[\![\boldsymbol{U}]\!]} + \frac{\partial z}{\partial \xi}\frac{\partial \chi}{\partial \tau}\right]\right)\Bigg|_{shock}. \tag{40}$$

Here, the commutative property of the ξ and τ derivatives is utilized.

Equations 39 and 40 both utilize the jump conditions of the conserved quantities. Note that any component of the flux vectors, $\boldsymbol{f}_\chi$ and $\boldsymbol{f}_z$, and the respective original conserved quantity, $\boldsymbol{U}$, can be used. In this paper, the energy jump condition is chosen as it includes all the other conserved quantities within it. Moreover, from the jump conditions, the normal detonation speed, D_N, can be calculated as

$$D_N = \left(\frac{[\![-\boldsymbol{f}_\chi \frac{\partial z}{\partial \xi} + \boldsymbol{f}_z \frac{\partial \chi}{\partial \xi}]\!]}{[\![\boldsymbol{U}]\!]\sqrt{\frac{\partial \chi}{\partial \xi}^2 + \frac{\partial z}{\partial \xi}^2}}\right)\Bigg|_{shock}. \tag{41}$$

3.3. Spatial Discretization

When the governing equations (Eqn. 34) are written in the succinct form as

$$\frac{\partial \boldsymbol{w}}{\partial \tau} + \frac{\partial \boldsymbol{f}_\xi}{\partial \xi} + \frac{\partial \boldsymbol{f}_\eta}{\partial \eta} = \boldsymbol{\mathcal{S}}, \tag{42}$$

it is more clear why the method of lines approach, which allows the spatial and temporal discretizations to be treated separately, is utilized. In this section, the point-wise spatial discretization and the approach used to approximate the flux and source terms are presented. Applying this semi-discretization to the solution, $\boldsymbol{w}(\xi, \eta, \tau)$, yields $\boldsymbol{w}_{i,j}(\tau)$, where the i and j are the spatial nodes in the ξ and $\eta-$directions, respectively.

In this work, a uniform Cartesian grid in the transformed space is used to discretize the spatial domain. In the $\xi-$direction, $N_\xi + 1$ points are spaced between ξ_l and ξ_r. Likewise in the η direction, $N_\eta + 1$ nodes are used such that $\eta_0 = \eta_{\min}$ and $\eta_{N_\eta} = 0$. The use of such a grid permits separate approximations in each direction for the flux derivatives as well as the inclusion of source terms.

The choice of using separate approximations for each direction yields several different classes of nodes in this spatial discretization. There are five such different regions: internal nodes, nodes near the shock front, nodes near the material interface, nodes near both, and ghost nodes. Figure 3 demonstrates the different types of nodes for a domain that is symmetric about $\xi_l = 0$. Ghost nodes near the rear outflow boundary are always used; whereas those near the side boundary are only used when a symmetric boundary condition is used.

3.3.1. Internal Nodes

The majority of the domain is composed of interior nodes. For these nodes, the gradient in both spatial directions are approximated using a Lax-Friedrichs scheme in conjunction with a fifth-order mapped weighted essentially non-oscillatory (WENO5M) scheme [15], in a similar manner to [16]. Within the interior of the domain, both non-fitted discontinuities, *e.g.* discontinuities in the derivative from applying zero gradient conditions at the rear boundary (Section 3.3.5) or secondary shocks, and singularities such as Prandtl-Meyer fans are possible. Thus, a conservative scheme which assures that captured discontinuities propagate at the correct speeds and eliminates several stability issues associated with simpler high-order finite-difference schemes such as WENO5M is necessary. In this section, this scheme will be laid out fully for the ξ direction derivatives; this same procedure is also applied in the η direction while along curves of constant ξ.

The Lax-Friedrichs flux splitting technique separates the derivative into contributions emanating from the right and left moving waves. Therefore,

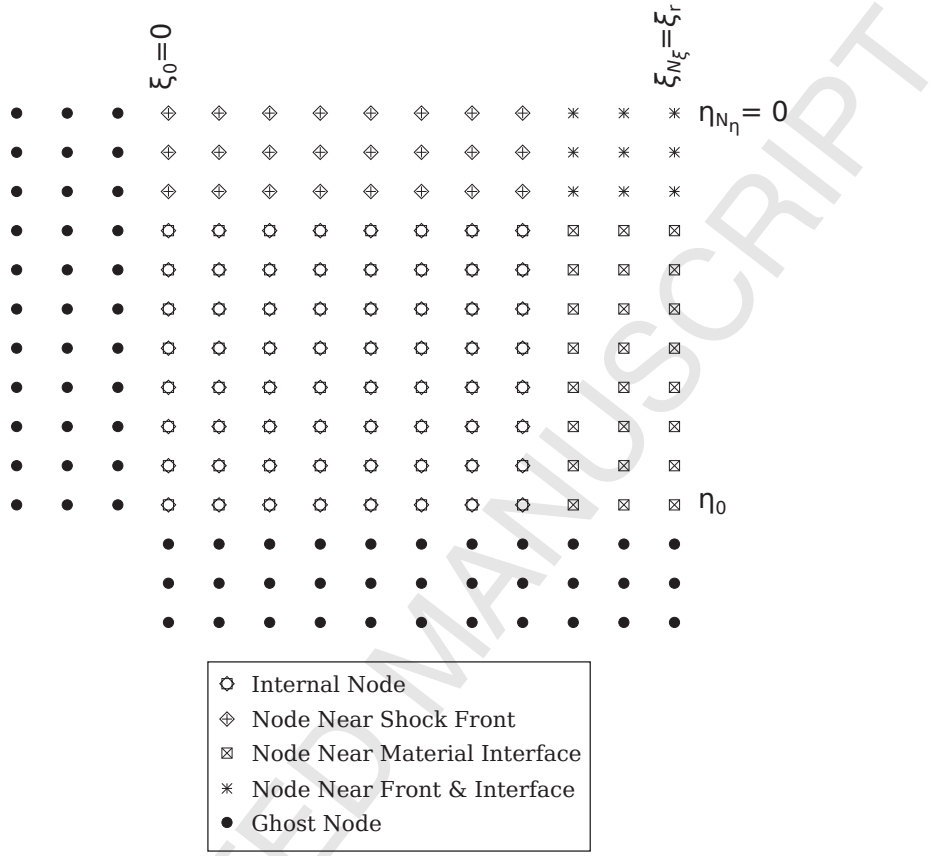

Figure 3
An example of a numerical grid demonstrating the various regions of the spatial discretization.

the spatial flux derivative in ξ direction can be written as

$$\left.\frac{\partial \boldsymbol{f}}{\partial \xi}\right|_{i,j} = \frac{1}{2}\left(\frac{\partial \boldsymbol{f}^{+}}{\partial \xi} + \frac{\partial \boldsymbol{f}^{-}}{\partial \xi}\right)\Bigg|_{i,j}, \tag{43}$$

where $\boldsymbol{f} \equiv \boldsymbol{f}_{\xi}$ and

$$\boldsymbol{f}^{\pm}_{i,j} = \boldsymbol{f}_{i,j} \pm \alpha \boldsymbol{w}_{i,j} \tag{44}$$

and α is the magnitude of largest local wave speed and the subscripts i and j indicate evaluation at the nodal point $\xi_i = \xi_0 + i\Delta\xi$ and $\eta_j = \eta_0 + j\Delta\eta$, respectively. The wave speeds are evaluated using the magnitudes of the eigenvalues of the Jacobian matrix, $\frac{\partial \mathbf{f}}{\partial \boldsymbol{w}}$.

Next, by utilizing the numerical flux function in a manner similar to [17, 15] and then applying the WENO5M scheme of [15, 10] to the right and left moving waves yields

$$\left.\frac{\partial \boldsymbol{f}^{\pm}}{\partial \xi}\right|_{i,j} = \frac{\hat{\boldsymbol{f}}^{\pm}_{i+\frac{1}{2},j} - \hat{\boldsymbol{f}}^{\pm}_{i-\frac{1}{2},j}}{\Delta\xi} + O\left(\Delta\xi^5\right), \tag{45}$$

where the approximations of numerical flux functions are given by the following stencils

$$\hat{\boldsymbol{f}}^{+}_{i+\frac{1}{2},j} = \mathcal{F}\left(\boldsymbol{f}^{+}_{i-2,j}, \boldsymbol{f}^{+}_{i-1,j}, \boldsymbol{f}^{+}_{i,j}, \boldsymbol{f}^{+}_{i+1,j}, \boldsymbol{f}^{+}_{i+2,j}\right), \tag{46}$$

$$\hat{\boldsymbol{f}}^{-}_{i+\frac{1}{2},j} = \mathcal{F}\left(\boldsymbol{f}^{-}_{i+3,j}, \boldsymbol{f}^{-}_{i+2,j}, \boldsymbol{f}^{-}_{i+1,j}, \boldsymbol{f}^{-}_{i,j}, \boldsymbol{f}^{-}_{i-1,j}\right). \tag{47}$$

As this procedure is applied to curves of constant η, the j position remains constant; thus, the j subscript will be discarded from this point forward.

Now, the WENO5M interpolator, developed by [15], is presented in further detail for a single right moving wave contribution flux, f^+. This interpolator is composed of three sub-stencils, q_k, and weights, ω_k, and is given by

$$\hat{f}^{+}_{i+\frac{1}{2}} = \mathcal{F}\left(f^{+}_{i-2}, f^{+}_{i-1}, f^{+}_{i}, f^{+}_{i+1}, f^{+}_{i+2}\right) = \sum_{k=1}^{3} \omega_k q_k. \tag{48}$$

The component stencils are defined as

$$q_1 = \frac{1}{6}\left(2f^{+}_{i-2} - 7f^{+}_{i-1} + 11f^{+}_{i}\right), \tag{49}$$

$$q_2 = \frac{1}{6}\left(-f^{+}_{i-1} + 5f^{+}_{i} + 2f^{+}_{i+1}\right), \tag{50}$$

$$q_3 = \frac{1}{6}\left(2f^{+}_{i} + 5f^{+}_{i+1} - f^{+}_{i+2}\right). \tag{51}$$

Following the procedure of [15], the weights first developed by [18], which are given by

$$\omega^{*}_{k} = \upsilon_k / \sum_{i=1}^{3} \upsilon_i, \quad \text{where} \quad \upsilon_k = \frac{\overline{\omega}_k}{\left(\epsilon + \beta_k\right)^2}, \tag{52}$$

are mapped in order to increase the accuracy of the scheme near critical points to fifth-order by

$$\omega_k = \frac{g_k\left(\omega_k^*\right)}{\sum_{i=1}^{3} g_i\left(\omega_i^*\right)}, \quad \text{where} \quad g_k\left(\omega\right) = \frac{\omega\left(\overline{\omega}_k + \overline{\omega}_k^2 - 3\overline{\omega}_k\omega + \omega^2\right)}{\overline{\omega}_k^2 + \left(1 - 2\overline{\omega}_k\right)\omega}. \tag{53}$$

Here $\overline{\omega}_k$ are the ideal weights for smooth regions $(\overline{\omega}_1 = 1/10, \overline{\omega}_2 = 6/10, \overline{\omega}_3 = 3/10)$, β_k are the smoothness indicators and ϵ is a small parameter which keeps the weights bounded. In this work $\epsilon = 10^{-40}$ as suggested in [15] and utilized by [10]. The three smoothness indicators for the WENO5M interpolator are defined as

$$\beta_1 = \frac{13}{12}\left(f_{i-2}^+ - 2f_{i-1}^+ + f_i^+\right)^2 + \frac{1}{4}\left(f_{i-2}^+ - 4f_{i-1}^+ + 3f_i^+\right)^2, \tag{54}$$

$$\beta_2 = \frac{13}{12}\left(f_{i-1}^+ - 2f_i^+ + f_{i+1}^+\right)^2 + \frac{1}{4}\left(-f_{i-1}^+ + f_{i+1}^+\right)^2, \tag{55}$$

$$\beta_3 = \frac{13}{12}\left(f_i^+ - 2f_{i+1}^+ + f_{i+2}^+\right)^2 + \frac{1}{4}\left(3f_i^+ - 4f_{i+1}^+ + f_{i+2}^+\right)^2, \tag{56}$$

$$\tag{57}$$

Using this scheme, Eqn. 43 for the derivative in the ξ direction can be expressed as

$$\begin{aligned}
\left.\frac{\partial \boldsymbol{f}}{\partial \xi}\right|_{i,j} &= \frac{1}{2}\left(\frac{\hat{\boldsymbol{f}}_{i+\frac{1}{2},j}^+ - \hat{\boldsymbol{f}}_{i-\frac{1}{2},j}^+}{\Delta\xi} + \frac{\hat{\boldsymbol{f}}_{i+\frac{1}{2},j}^- - \hat{\boldsymbol{f}}_{i-\frac{1}{2},j}^-}{\Delta\xi}\right) + O\left(\Delta\xi^5\right), \\
&= \frac{1}{\Delta\xi}\left(\frac{\hat{\boldsymbol{f}}_{i+\frac{1}{2},j}^+ - \hat{\boldsymbol{f}}_{i+\frac{1}{2},j}^-}{2} + \frac{\hat{\boldsymbol{f}}_{i+\frac{1}{2},j}^+ - \hat{\boldsymbol{f}}_{i-\frac{1}{2},j}^-}{2}\right) + O\left(\Delta\xi^5\right), \\
&= \frac{\hat{\boldsymbol{f}}_{i+\frac{1}{2},j} - \hat{\boldsymbol{f}}_{i-\frac{1}{2},j}}{\Delta\xi} + O\left(\Delta\xi^5\right).
\end{aligned} \tag{58}$$

There is now a single approximate numerical flux defined at the midpoints between the nodes; as an illustrative example this flux approximation between the i and $i+1$ nodes is given by

$$\hat{\boldsymbol{f}}_{i+\frac{1}{2},j} = \frac{1}{2}\left(\hat{\boldsymbol{f}}_{i+\frac{1}{2},j}^+ - \hat{\boldsymbol{f}}_{i+\frac{1}{2},j}^-\right). \tag{59}$$

To obtain the approximation at the other necessary location for the derivative calculation, $i-1/2$, one must only shift Eqn. 59 by a single node, to the nodes $i-1$ and i.

At internal nodes, there are no boundary conditions to be dealt with and thus, the only governing equations are given by Eqn. 42. Therefore, applying this spatial discretization to the governing equations yields

$$\frac{d\boldsymbol{w}_{i,j}}{dt} = -\left(\frac{\hat{\boldsymbol{f}}_\xi\Big|_{i+\frac{1}{2},j} - \hat{\boldsymbol{f}}_\xi\Big|_{i-\frac{1}{2},j}}{\Delta\xi}\right) - \left(\frac{\hat{\boldsymbol{f}}_\eta\Big|_{i,j+\frac{1}{2}} - \hat{\boldsymbol{f}}_\eta\Big|_{i,j-\frac{1}{2}}}{\Delta\eta}\right) + \boldsymbol{\mathcal{S}}\left(\boldsymbol{w}_{i,j}\right) + O\left(\Delta\xi^5\right) + O\left(\Delta\eta^5\right), \quad (60)$$

where $\boldsymbol{\mathcal{S}}\left(\boldsymbol{w}_{i,j}\right)$ is simply the source term evaluated at the nodal point ξ_i, η_j. For nodes near the boundaries, a different discretization must be used such that only points within the domain or the boundary conditions themselves are utilized. These different discretizations are detailed in the following sections.

3.3.2. Nodes Near the Shock Front

For the two nodes directly behind the fitted shock, the flux derivatives in the η direction are approximated using formulas developed using Taylor series expansions involving nodes up to and including the shock front. These derivative approximations are given by

$$\left.\frac{\partial \boldsymbol{f}_\eta}{\partial\eta}\right|_{i,N_\eta-2} \approx \frac{1}{12\Delta\eta}\left(\boldsymbol{f}_\eta\big|_{i,N_\eta-4} - 8\,\boldsymbol{f}_\eta\big|_{i,N_\eta-3} + 8\,\boldsymbol{f}_\eta\big|_{i,N_\eta-1} - \boldsymbol{f}_\eta\big|_{i,N_\eta}\right), \quad (61)$$

$$\left.\frac{\partial \boldsymbol{f}_\eta}{\partial\eta}\right|_{i,N_\eta-1} \approx \frac{1}{12\Delta\eta}\Big(-\boldsymbol{f}_\eta\big|_{i,N_\eta-4} + 6\,\boldsymbol{f}_\eta\big|_{i,N_\eta-3} - 18\,\boldsymbol{f}_\eta\big|_{i,N_\eta-2} + 10\,\boldsymbol{f}_\eta\big|_{i,N_\eta-1} + 3\,\boldsymbol{f}_\eta\big|_{i,N_\eta}\Big). \quad (62)$$

Both of these approximations are only fourth-order accurate. The use of these stencils are necessary to ensure numerical stability of the scheme; however, as stated in [10], this scheme does appear to retain its global fifth-order convergence rate in the spatial domain, due to the fact that Eqns. 61-62 are not applied along a characteristic, as demonstrated in Sections 4.1 and 4.2 for several examples.

Now, the velocity at which the fitted discontinuity (shock) moves is dictated by the jump in the flow from the ambient upstream to the shocked state in the normal direction. Therefore, the solution at the shock front, $j = N_\eta$, is a function of the flow as well as the shock shape, $\partial z_s/\partial \xi$. More succinctly, the front state must satisfy the normal Rankine-Hugoniot conditions.

In order to satisfy these conditions, the normal shock speed is first determined using the energy equation of the Euler equations in conjunction with Eqn. 41. Since the jump condition for each conserved quantity is equivalent, one may choose any of the jump conditions. The energy equation is chosen for this work as it takes into account all of the state variables and the shock shape. Using the normal shock speed, the shock state is then calculated by

$$\rho_s \left(u_{N_s} - D_N\right) = \rho_0 \left(u_{N_0} - D_N\right), \tag{63}$$

$$p_s - p_0 = \left(\rho_0 \left(u_{N_0} - D_N\right)\right)^2 \left(\frac{1}{\rho_0} - \frac{1}{\rho_s}\right), \tag{64}$$

$$e_s - e_0 = \frac{1}{2}\left(p_s + p_0\right)\left(\frac{1}{\rho_0} - \frac{1}{\rho_s}\right), \tag{65}$$

$$\lambda_s = \lambda_0, \tag{66}$$

$$u_{T_s} = u_{T_0}, \tag{67}$$

where u_N, u_T are the normal and tangent velocity, respectively. The subscripts s and 0 denote the shock and ambient states, respectively. Lastly, the flow is evolved in time at the front with the flux derivatives in the η direction approximated by the fifth-order accurate one-sided finite difference scheme given by

$$\begin{aligned}\left.\frac{\partial \boldsymbol{f}_\eta}{\partial \eta}\right|_{i,N_\eta} \approx \frac{1}{60\Delta\eta}\Big(&-12\left.\boldsymbol{f}_\eta\right|_{i,N_\eta-5} + 75\left.\boldsymbol{f}_\eta\right|_{i,N_\eta-4} - 200\left.\boldsymbol{f}_\eta\right|_{i,N_\eta-3} \\ &+300\left.\boldsymbol{f}_\eta\right|_{i,N_\eta-2} - 300\left.\boldsymbol{f}_\eta\right|_{i,N_\eta-1} + 137\left.\boldsymbol{f}_\eta\right|_{i,N_\eta}\Big).\end{aligned} \tag{68}$$

The evaluation of ξ flux derivatives in both Eqns. 40 and 42 utilizes the same WENO5M scheme presented for the internal nodes in Section 3.3.1, except near the material interfaces, which will be discussed later in Section 3.3.3. Furthermore, the source terms are once again simply evaluated at the nodal points of $(i, N_\eta - 2)$ and $(1, N_\eta - 1)$; however, at (i, N_η) the shock jump conditions are enforced.

In addition, the shock front location at the center of the HE is also updated using Eqn. 39 which is treated as an ODE in time with the spatial

component evaluated at the node. The rest of the front locations are constructed purely for plotting purposes *a posteriori*. By utilizing the fact that the shock front is a function only of ξ, the shock shape can be calculated by

$$z_s(\xi) = z_{s_{CL}} + \int_{\xi_{CL}}^{\xi} \frac{dz_s}{d\hat{\xi}} d\hat{\xi}, \tag{69}$$

where $z_{s_{CL}}$ is the shock front location at the center of the HE (ξ_{CL}). Here, this integral is approximated using the second-order accurate trapezoidal method.

3.3.3. Material Interface Nodes

Near the material interfaces, flux derivatives in the ξ direction are approximated using lower-order accurate and simpler stencils which are biased to include only nodes within the computational domain. Near the left material interface $(i = 0)$, these are given by

$$\left.\frac{\partial \boldsymbol{f}_\xi}{\partial \xi}\right|_{0,j} \approx \frac{1}{\Delta\xi}\left(-\left.\boldsymbol{f}_\xi\right|_{0,j} + \left.\boldsymbol{f}_\xi\right|_{1,j}\right), \tag{70}$$

$$\left.\frac{\partial \boldsymbol{f}_\xi}{\partial \xi}\right|_{1,j} \approx \frac{1}{2\Delta\xi}\left(-\left.\boldsymbol{f}_\xi\right|_{0,j} + \left.\boldsymbol{f}_\xi\right|_{2,j}\right), \tag{71}$$

$$\left.\frac{\partial \boldsymbol{f}_\xi}{\partial \xi}\right|_{2,j} \approx \frac{1}{2\Delta\xi}\left(-\left.\boldsymbol{f}_\xi\right|_{1,j} + \left.\boldsymbol{f}_\xi\right|_{3,j}\right), \tag{72}$$

and near the right material interface $(i = N_\xi)$, these are given by

$$\left.\frac{\partial \boldsymbol{f}_\xi}{\partial \xi}\right|_{N_\xi-2,j} \approx \frac{1}{2\Delta\xi}\left(-\left.\boldsymbol{f}_\xi\right|_{N_\xi-3,j} + \left.\boldsymbol{f}_\xi\right|_{N_\xi-1,j}\right), \tag{73}$$

$$\left.\frac{\partial \boldsymbol{f}_\xi}{\partial \xi}\right|_{N_\xi-1,j} \approx \frac{1}{2\Delta\xi}\left(-\left.\boldsymbol{f}_\xi\right|_{N_\xi-2,j} + \left.\boldsymbol{f}_\xi\right|_{N_\xi,j}\right), \tag{74}$$

$$\left.\frac{\partial \boldsymbol{f}_\xi}{\partial \xi}\right|_{N_\xi,j} \approx \frac{1}{\Delta\xi}\left(-\left.\boldsymbol{f}_\xi\right|_{N_\xi-1,j} + \left.\boldsymbol{f}_\xi\right|_{N_\xi,j}\right). \tag{75}$$

At the material interfaces, the scheme is a first-order one-sided difference Taylor-series expansion. At the neighboring points, the standard second-order central difference scheme is utilized. These lower-order accurate Taylor-series approximations are utilized near the material interfaces for numerical

stability purposes, as a self-similar Prandtl-Meyer expansion fan may form requiring robust solution techniques. These approximations reduce the local rate of convergence of the scheme; however, the denotation velocity (and thus the shock state) still convergences at high-order as demonstrated in Sections 4 and 5.1. This is a consequence of the domain of dependence for the shock front behavior given the particular problems of interest in this work. This domain is roughly approximated by the sonic locus, which is discussed further in Section 5.1.

In addition, the flow must be parallel to the material interfaces. In order to enforce the velocity be tangent to the interfaces, the normal velocity of the flow must be set to the velocity of the interfaces, $\partial\chi/\partial\tau\big|_{\chi_l}$ or $\partial\chi/\partial\tau\big|_{\chi_r}$. This is accomplished by correcting the χ direction velocity in the shock-attached frame at the interface using the following

$$u_\chi = \left(\frac{\frac{\partial\chi}{\partial\eta}}{\frac{\partial z}{\partial\eta}}\right)\left(u_z - \frac{\partial z}{\partial\tau}\right) + \frac{\partial\chi}{\partial\tau}. \tag{76}$$

3.3.4. Symmetric Boundary Nodes

In the case where the deflection of the material interfaces are symmetric, the computational domain can be reduced to half of the full domain in the slab geometry. In order to accomplish this, three ghost (extra) cells are used in the ξ direction to enforce the null flow and flux conditions across the boundary at $\xi = 0$. At these ghost cells the state variables take a value equivalent to that of a cell equidistant from the symmetry plane except for the velocity perpendicular to the symmetry plane which is equal in magnitude but in the opposite direction. As an example for a ghost node to the immediate left of the symmetry plane shown in Fig. 3, $i = -1$, this can be accomplished by

$$\begin{aligned} &\rho|_{-1,j} = \rho|_{1,j}\,, \quad u_x|_{-1,j} = -\,u_x|_{1,j}\,, \quad u_z|_{-1,j} = u_z|_{1,j}\,, \\ &e_t|_{-1,j} = e_t|_{1,j}\,, \quad \lambda|_{-1,j} = \lambda|_{1,j}\,, \quad \left.\frac{\partial z}{\partial\xi}\right|_{-1,j} = \left.\frac{\partial z}{\partial\xi}\right|_{1,j}; \end{aligned} \tag{77}$$

this same procedure is also applied for ghost nodes $i = -2$ and $i = -3$. Using these ghost nodes, the ξ flux derivatives can be calculated using the WENO5M scheme developed in Section 3.3.1 for all points up to and including the plane of symmetry ($\xi = 0$) .

Although the physical nature of the axisymmetric case is different, the same null flow and flux conditions at $\xi = 0$ are true; as such, the same ghost

cell procedure in the ξ direction is applied in this case as well. In addition to these conditions, care must also be taken for the source terms emanating from the axisymmetric nature at $r = 0$ as they all include a denominator of r. The numerators of these source terms are also zero at $r = 0$ due the null flow condition at the symmetry line. Therefore to evaluate what these source terms should be at $r = 0$, L'Hôpital's rule must be applied,

$$\lim_{r\to 0} \frac{-\rho u_r}{r} = \lim_{r\to 0} \frac{-\left(\rho \frac{\partial u_r}{\partial r} + \frac{\partial \rho}{\partial r} u_r\right)}{1} = \left(-\rho \frac{\partial u_r}{\partial r}\right)\bigg|_{r=0}, \tag{78}$$

$$\lim_{r\to 0} \frac{-\rho u_r u_r}{r} = \lim_{r\to 0} \frac{-\left(2\rho \frac{\partial u_r}{\partial r} u_r + \frac{\partial \rho}{\partial r} u_r u_r\right)}{1} = 0, \tag{79}$$

$$\lim_{r\to 0} \frac{-\rho u_r u_z}{r} = \lim_{r\to 0} \frac{-\left(\rho u_z \frac{\partial u_r}{\partial r} + \frac{\partial}{\partial r}\left(\rho u_z\right) u_r\right)}{1} = \left(-\rho u_z \frac{\partial u_r}{\partial r}\right)\bigg|_{r=0}, \tag{80}$$

$$\lim_{r\to 0} \frac{-\left(\rho e_t + p\right) u_r}{r} = \left(-\left(\rho e_t + p\right) \frac{\partial u_r}{\partial r}\right)\bigg|_{r=0}, \tag{81}$$

$$\lim_{r\to 0} \frac{-\rho \lambda u_r}{r} = \left(-\rho \lambda \frac{\partial u_r}{\partial r}\right)\bigg|_{r=0}. \tag{82}$$

Here, the zero radial velocity at the centerline of the HE is applied. Recall, that the source terms in Eqn. 78-82 are also mapped into the computational domain by multiplying by $\sqrt{g}$; therefore, using Eqns. 33 and the chain rule allows for the continuity source term along the centerline to be written as

$$\left(-\sqrt{g}\rho \frac{\partial u_r}{\partial r}\right)\bigg|_{r=0} = \left[-\rho\left(\frac{\partial u_r}{\partial \xi}\frac{\partial z}{\partial \eta} - \frac{\partial u_r}{\partial \eta}\frac{\partial z}{\partial \xi}\right)\right]\bigg|_{\xi=0}. \tag{83}$$

Likewise, this same procedure can be applied to the remaining source terms at the centerline. In the current transformated construction, $\partial z/\partial \eta = 1$ and $\partial z/\partial \xi|_{\xi=0} = 0$; therefore, these source terms are only dependent on $\partial u_r/\partial \xi|_{\xi=0}$. This term of $\partial u_r/\partial \xi|_{\xi=0}$ is approximated using a sixth-order central difference stencil assuming a symmteric nature of the velocity, such that

$$\left.\frac{\partial u_r}{\partial \xi}\right|_{\xi=0,\eta=\eta_j} \approx \frac{45\ u_r|_{1,j} - 9\ u_r|_{2,j} + u_r|_{3,j}}{30\Delta\xi}. \tag{84}$$

3.3.5. Rear Boundary Nodes

As mentioned previously, at the rear boundary, a zero gradient condition in the η direction is enforced. This is accomplished by making use of a set

of three ghost nodes in the η direction behind the last point in the computational domain as shown in Fig. 3. The state variables for these nodes are set equal to that of the last node in the computational domain. Then, the η flux derivative at the rear boundary can be calculated using the WENO5M scheme developed in Section 3.3.1. The use of such a boundary condition causes minimimal to no effect on the propagation of the detonation front if applied behind the sonic locus, which is shown in Fig. 1, as information about the flow behind this curve propagates away from the front.

3.4. Temporal Integration

After applying the spatial discretization described previously and evaluating the source terms, one is left with a set of ordinary differential equations (ODEs) in time at each i, j node, such that

$$\frac{d\boldsymbol{w}_{i,j}}{d\tau} = \boldsymbol{L}\left(\boldsymbol{w}\right)|_{\xi=\xi_i,\eta=\eta_j}, \tag{85}$$

where $\boldsymbol{L}$ is the discrete approximation to the fluxes and source terms. Therefore, these ODEs can be solved using a wide variety of integration schemes.

In this work, the ODEs are solved by an explicit RK scheme. In general, RK schemes integrate a given solution from an initial time, τ_n, to an incrementally larger time, $\tau_{n+1} = \tau_n + \Delta\tau_n$, using several intermediary steps. Following a similar notation to that of [10], this procedure can be written for an initial solution of $\boldsymbol{w}_{i,j}^n$ at τ_n for a s-stage scheme as

$$\bar{\boldsymbol{w}}_{i,j}^1 = \boldsymbol{w}_{i,j}^n, \tag{86}$$

$$\bar{\boldsymbol{w}}_{i,j}^l = \boldsymbol{w}_{i,j}^n + \Delta\tau_n \sum_{k=1}^{l-1} a_{lk} \boldsymbol{L}\left(\bar{\boldsymbol{w}}_{i,j}^k\right), \tag{87}$$

$$\boldsymbol{w}_{i,j}^{n+1} = \boldsymbol{w}_{i,j}^n + \Delta\tau_n \sum_{k=1}^{s} b_k \boldsymbol{L}\left(\bar{\boldsymbol{w}}_{i,j}^k\right), \tag{88}$$

where $\bar{\boldsymbol{w}}_{i,j}^l$ are the solutions at the intermediary stage l, and a_{lk} and b_k are integration coefficients. These coefficients for the two schemes used in this work, the three stage third-order accurate scheme extracted from [17] and the six stage fifth-order accurate scheme adopted from [19], are given in Tables 1 and 2, respectively. Here, the temporal discretization is determined by the fastest advection speed in one direction as the effects of the

source terms are fully resolved. This uni-directional time-step is then multiplied by a Courant−Friedrichs−Lewy (CFL) number of 4/5 to maintain the numerical stability of the integration scheme; then to compensente for the multi-dimensional nature of the scheme, this value is divided by 2 to give the overall temporal discretization size. Moreover, small changes in the CFL number do not effect the results presented.

Table 1
Coefficients for a three stage third-order accurate Runge-Kutta scheme from [17]

k	a_{k1}	a_{k2}	b_k
1			$\frac{1}{6}$
2	1		$\frac{1}{6}$
3	$\frac{1}{4}$	$\frac{1}{4}$	$\frac{2}{3}$

Table 2
Coefficients for a six stage fifth-order accurate Runge-Kutta scheme from [19]

k	a_{k1}	a_{k2}	a_{k3}	a_{k4}	a_{k5}	b_k
1						$\frac{1}{24}$
2	1					0
3	$\frac{1}{4}$	$\frac{1}{4}$				0
4	$\frac{2046}{15625}$	$-\frac{454}{15625}$	$\frac{1533}{15625}$			$\frac{125}{336}$
5	$-\frac{739}{5625}$	$-\frac{511}{5625}$	$-\frac{566}{5625}$	$\frac{20}{27}$		$\frac{27}{56}$
6	$\frac{11822}{21875}$	$-\frac{6928}{21875}$	$-\frac{4269}{21875}$	$-\frac{4}{7}$	$\frac{54}{35}$	$\frac{5}{48}$

4. Verification

During the development of any new scheme, it is important to verify the accuracy of the numerical implementation and the governing equations with several test problems. The test problems utilized here are a decaying planar non-reacting shock wave (Sedov-Taylor blast wave), a planar steadily propagating detonation wave, and steady flow around symmetrical right cone at zero angle of attack (Taylor-Maccoll flow). The first example verifies that

the time-dependent nature of an inert flow is captured correctly at a high-order convergence rate. Furthermore, the implementation of the reaction source term is verified by the steadily traveling detonation wave. The Taylor-Maccoll flow is exploited to verify the spatial convergence rate of a solution that exercises the axisymmetric based source terms.

4.1. Planar Sedov-Taylor Blast Wave

The intense explosion in a perfect gas is valuable for verification as the flow can be reduced to a similarity solution. The theoretical development for these blast waves was first demonstrated by [20, 21, 22]. The solution assumes an uniform PF-CAE initially at rest in which a large amount of energy, E, is deposited at an initial time, $t = 0$. This generates a blast wave with a leading shock that is a function of time at a distance from the origin, $\mathsf{R}(t)$. Behind this shock the flow is isentropic when diffusive effects and body forces are neglected in the flow. This similarity solution, given by Eqn. B.43 (as well as others given in Appendix B), maintains the same shape for all time in terms of a nondimensional radius, ζ. Furthermore, this transcendental equation that can be solved up to an arbitrary accuracy allowing for a detailed comparison and a calculation of errors.

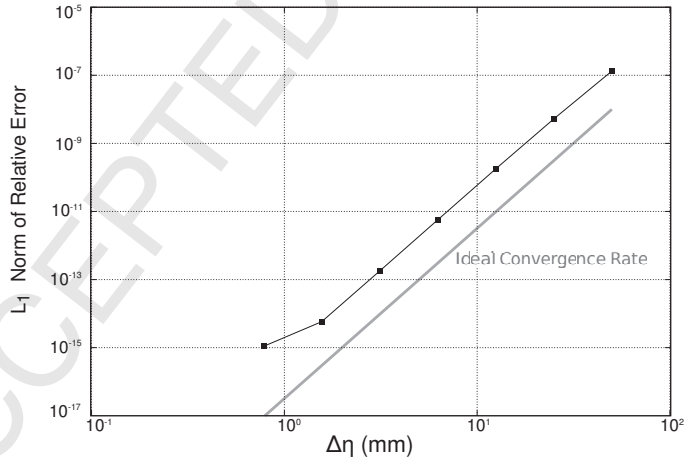

Figure 4
A log-log plot of the L_1-norm of the relative error at $t = 1.00202\ \mu s$ for the total energy versus the resolution of the simulation.

For this test case, the blast wave is initialized by plane of instantaneous energy, $\mathsf{E} = 7.02912 \times 10^6\ J/mm^2$, deposited into an quiescent PF-CAE with

$\gamma = 1.4$ and $\rho_o = 1.25{\times}10^{-3}\ mg/mm^3$, resulting in an one-dimensional Cartesian wave that decays in strength with repsect to time in the physical domain. The test case is initialized at $t = 1\ \mu s$ using the exact solution obtained by inverting Eqn. B.43. The total length of the physical domain is $L_z = 2000\ mm$ and it starts from the blast radius, $\mathsf{R}\,(t = 1\ \mu s) \approx 2197.0134\ mm$. The temporal integration is accomplished using the fifth-order RK method presented in Section 3.4.

The L_1-norm for the relative error over the front half of the domain in the localized total energy, ρe_t, at $t = 1.00202\ \mu s$ are shown versus the resolution of the simulation in Fig. 4. The relative error is only calculated over half of the domain nearest the shock, as there is $\mathcal{O}\,(1)$ error from applying the constant gradient back boundary condition to the Sedov−Taylor blast wave flow. The slope of this curve in the log-log space indicates the solution is converging at a rate of 4.95, which is nearly the ideal fifth-order rate of the scheme. Table 3 lists the L_1 error norm at each resolution and the local convergence rates. The solution of the finest resolution of $\Delta\eta = 0.78125\ mm$ is affected by round-off error. This round-off error is what causes the convergence rate of the solution to diverge from the ideal fifth-order convergence at fine grids.

Table 3
L_1 error in the total energy in Sedov−Taylor blast wave flow

Resolution (mm)	L_1-error norm	r_c
50.00000	1.3322×10^{-7}	-
25.00000	5.2527×10^{-9}	4.665
12.50000	1.7988×10^{-10}	4.868
6.25000	5.6866×10^{-12}	4.983
3.12500	1.7943×10^{-13}	4.986
1.56250	5.8144×10^{-15}	4.948
0.78125	1.0951×10^{-15}	2.409

4.2. Steady Planar Detonations

A CJ detonation propagating in an idealized HE has been shown to relax to a stable, self-sustained, steadily-traveling wave for certain conditions. This stability has been demonstrated both numerically [10] and using linear stability theory [23]. The stability of one of these detonations offers the ability

to check that the shock-speed is being correctly predicted by the algorithm and that the reaction source term is correctly implemented.

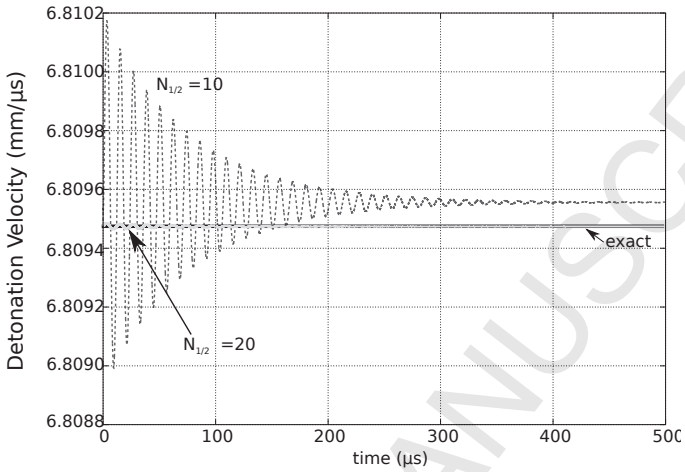

Figure 5
Detonation velocity versus time curves for resolutions with $N_{1/2} = 10$ and $N_{1/2} = 20$ versus the exact solution of a PF-CAE.

For this verification example, the same set of non-dimensional standard parameters used by [10] is chosen so that a stable detonation is realized. Thus for this case, a PF-CAE with an ambient density of $\rho_o = 1$, ambient pressure of $p_o = 1$, and a constant ratio of specific heats of $\gamma = 1.2$ is utilized. The heat release of the reaction is $q = 50$. With these ambient conditions and heat release, the CJ detonation velocity can be calculated :

$$D_{CJ} = \sqrt{\frac{\gamma p_o}{\rho_o} + \frac{q\left(\gamma^2 - 1\right)}{2}} + \sqrt{\frac{q\left(\gamma^2 - 1\right)}{2}} \approx 6.80947463. \tag{89}$$

By using the remaining reaction parameters detailed here, the reaction rate scale factor $a = 35.955584760859722$, the pressure scaling factor $B = 1$, the pressure dependence exponent $N_p = 0$, the depletion exponent $\nu = 1$, and lastly the activation energy of the reaction $E = 25$, gives rise to a steady, CJ detonation, with a half-reaction zone length of $L_{1/2} = 1$. The calculations presented are initialized using the steady ZND wave structure.

Figure 5 shows the calculated detonation velocity versus time for $\Delta\eta = \Delta\xi = 0.10$ and $\Delta\eta = \Delta\xi = 0.05$. These relatively coarse resolutions correspond to 10 and 20 points within the half-reaction zone length. The early

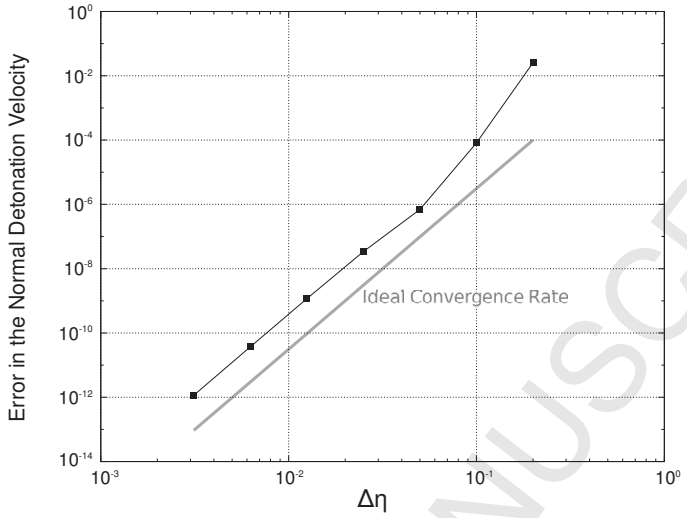

Figure 6
The late time error in the detonation velocity versus resolution for a stable, steadily propagating detonation in a PF-CAE.

time behavior is dominated by the small perturbations to the exact ZND due the discretization; however, at later times the detonation relaxes to a stable detonation as expected. The long time error in the steady detonation speed versus the resolution of the calculation is shown in Fig. 6. The slope of this log-log curve demonstrates that the rate of convergence for this scheme is ~ 5.01 except near the coarsest resolutions presented which have a rate of convergence which is greater than the nominal value for the scheme. At the finest resolution, the scheme comes close to the round-off error due the double-precision nature of the calculations. Figure 6 demonstrates clearly that even with moderate resolutions, the shock-fitting technique presented delivers highly accurate solutions while also offering a high-order convergence rate.

4.3. Taylor-Maccoll Flow

The steady, supersonic flow of a PF-CAE past a sharp symmetrical right semi-infinite cone at zero angle of attack can be reduced to a solution for a single variable in a similar manner to that in Section 4.1. In Taylor-Maccoll flow, the cone induces a leading shock emanating from the tip followed by flow which is continuously deflected downstream of the shock and eventually becomes asymptotically parallel to the surface at infinity. As such, the flow

is only dependent on the angle of inclination, θ, at a point in space; more explicitly, it is independent of the distance from the tip, l, and azimuthal angle, ϕ, from spherical coordinates centered at the tip of the cone. Therefore, it can be demonstrated that the flow properties remain constant along an individual ray from the vertex of the cone, with the flow properties varying continuously between rays. This flow field was first examined in a graphical form by [24]; later, a longer development of the governing equation and a numerical solution was presented by [25]. A numerical simulation of such a flow field verifies that axisymmetric based source terms properly capture the different geometrical configuration of the flow. This work utilizes the governing ODE developed for a PF-CAE by [26, Chap. 10] to initialize the flow field :

$$\frac{(\gamma-1)}{2}\left[2h_t - u_l^2 - \left(\frac{\partial u_l}{\partial \theta}\right)^2\right]\left[2u_l + \frac{\partial u_l}{\partial \theta}\cot\theta + \frac{\partial^2 u_l}{\partial \theta^2}\right] - \left(\frac{\partial u_l}{\partial \theta}\right)^2\left[u_l + \frac{\partial^2 u_l}{\partial \theta^2}\right] = 0. \quad (90)$$

Here, $h_t = h + u_0^2/2$, is the total enthalpy of the ambient flow, u_0 the ambient flow velocity, and u_l the radial velocity in spherical coordinates.

Table 4
Spatial error in continuity equation evaluation for the ($\xi = 0.3\ mm$, $\eta = -0.3\ mm$) point in Taylor-Maccoll Flow

$\Delta\eta = \Delta\xi$ (mm)	Double Precision $(mg/(mm^3\ s))$	r_c	Quad Precision $(mg/(mm^3\ s))$	r_c
0.100000000	3.77095×10^{-6}	-	3.77095×10^{-6}	-
0.050000000	9.76561×10^{-9}	8.593	9.76561×10^{-9}	8.593
0.025000000	3.55008×10^{-11}	8.104	3.54999×10^{-11}	8.104
0.012500000	1.16054×10^{-11}	1.613	1.16047×10^{-11}	1.613
0.006250000	4.72337×10^{-13}	4.620	4.71830×10^{-13}	4.620
0.003125000	1.61308×10^{-14}	4.911	1.56784×10^{-14}	4.911
0.001562500	5.18249×10^{-16}	4.963	5.02698×10^{-16}	4.963
0.000781250	2.98589×10^{-15}	-2.526	1.58693×10^{-17}	4.985
0.000390625	-	-	4.68001×10^{-19}	5.084

The conical flow problem chosen for this work is a Mach 1.84 flow in air

($\rho_0 = 1.25 \times 10^{-3}\ mg/mm^3$ and $p_0 = 1.01325 \times 10^{-4}\ GPa$) over cone with an half angle of 12.5° which results in a shock angle of $\sim 35.0816568099°$ and for which [27, Figure 259] presented a Schlieren image of an experiment. It is worth noting, that this verification problem yields a non-trivial Jacobian transformation, and it indeed activates the axisymmetric source terms as well as both ξ and η directional derivatives. Due to the singularity at the vertex of the cone, which tries to enforce both the shock and the cone surface, the simulation is unstable at finite times. However, this flow can still provide an useful verification of the spatial errors away from the vertex. Since the initial conditions for the simulation are calculated using the analytic steady solution, the spatial error can be calculated by evaluating the discrete operator which is used to approximate the fluxes and source terms, $\boldsymbol{L}\left(\bar{\boldsymbol{w}}_{i,j}^{k}\right)$. At points away from the tip of the cone, the rate of convergence is fifth-order given enough resolution; a typical point ($\xi = 0.3\ mm$, $\eta = -0.3\ mm$) is chosen to illustrate the rate of convergence of the spatial errors. Table 4 shows the spatial error for the continuity equation as well as the rates of convergence of the method for the usual double precision calculations and those for quad precision. As with the previous test cases, there is super-convergence observed at the coarser grids which is followed by the method approaching the asymptotic convergence rate. In the double precision case, the method hits round-off error at the finest grid examined but the rate of convergence is near the ideal rate. Moreover, when this same resolution is examined with quad precision the method still approaches the ideal convergence rate.

5. Applications

In this section, the shock-fitting method detailed here is applied to HEs in order to examine the steady-state phase speed. Two separate EOSs are examined; the first is the simpler PF-CAE model and the second is the WSD model. The PF-CAE EOS case will be compared with previously published model presented in [2]. Utilizing the WSD model both slab/axisymmetric rate-stick geometries are examined and thickness/diameter effect curves are produced for a published model of PBX 9501.

All cases presented are symmetric and initialized using the one-dimensional planar ZND profile for a detonation traveling at D_{CJ}. The material interface follows a prescribed motion; it is initially parallel to the one-dimensional ZND wave structure and deflects out to angle corresponding to an unconfined HE experiment and equivalently, to the maximum streamline deflection

of a single oblique shock. Here, the full form of the motion is given by

$$\chi_l(\eta,\tau) = \xi_l, \tag{91}$$

$$\chi_r(\eta,\tau) = \begin{cases} \xi_r - \eta m \sum_{i=6}^{11} a_i \left(\frac{\tau}{\tau_c}\right)^i & \frac{\tau}{\tau_c} < 1 \\ \xi_r - \eta m & \frac{\tau}{\tau_c} \geq 1 \end{cases}, \tag{92}$$

where m is the slope corresponding the deflection angle, a_i the polynomial constants, and τ_c a time constant. Choosing $a_6 = 462$, $a_7 = -1980$, $a_8 = 3465$, $a_9 = -3080$, $a_{10} = 1386$, and $a_{11} = -252$ gives a material interface deflection that is smooth and fives times smoothly differentiable in τ. The deflection angle is calculated by a shock polar analysis in the manner presented by [28] for the PF-CAE model and [29, 30] for the WSD model. With the main variable of interest being the steady-state phase speed, the third-order RK scheme is utilized for temporal integration as the main source of error is due to spatial discretization.

5.1. PF-CAE HE Slabs

A convergence study is performed examining the unconfined steady detonation phase speed and a comparison between shock-fitting and shock-capturing is made for a 48 mm wide slab of HE using a PF-CAE which weakly mimics PBX 9502. The PF-CAE/reaction model parameters are taken from [2] and are given by $\gamma = 3$, $q = 4\ mm^2/\mu s^2$, $\rho_0 = 2\ mg/mm^3$, $p_0 = 10^{-4}\ GPa$, $k = 1.2936\ 1/\mu s$, $\nu = 1/2$, $B = p_{CJ}$, $N = 2$, and $E = 0\ mm^2/\mu s^2$. With this choice of parameters, the Chapman-Jouguet detonation speed and pressure are $D_{CJ} \approx 8.00\ mm/\mu s$ and $p_{CJ} \approx 32.0\ GPa$, respectively.

The total reaction zone length is $\sim 4\ mm$ and the ZND solution is very near the strong shock limit. From shock polar theory, it is known that for a single oblique shock, there is an associated streamline deflection angle [26]. For a PF-CAE in the strong shock limit, this deflection angle can be calculated explicitly, $\phi_e = \arctan\left(\sqrt{(\gamma-1)/(\gamma+1)}\right) \approx 35.3°$. This corresponds to streamline turning angle of $\theta_e \approx 19.5°$. Likewise, it also corresponds to the flow being exactly sonic in the shock-attached reference frame. This turning angle yields $m \approx 0.35355$. The time constant chosen for material interface motion is $\tau_c = 5\ \mu s$. For ease of comparison with the previously preformed shock-capturing calculations, the computational domain length chosen is 10 mm.

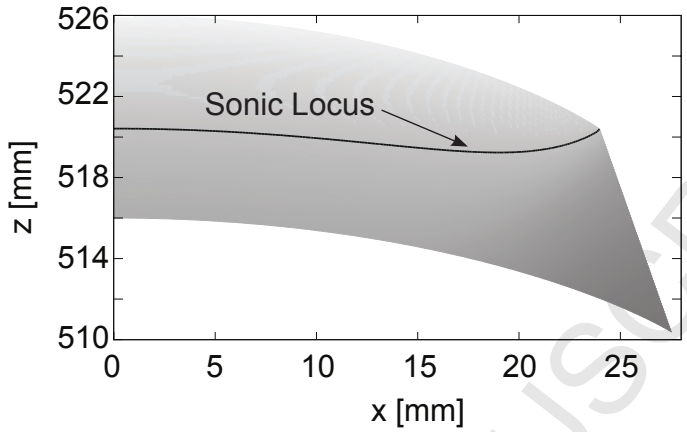

Figure 7
The predicted steady half-profile for the sonic parameter in a symmetric 48 mm wide slab for a PF-CAE HE at resolution of 1/8 mm. The sonic locus is denoted by the black curve.

Figure 7 shows the sonic parameter for the steady wave profile for resolution of 1/8 mm. The sonic parameter is defined as the local sound speed squared minus the magnitude of velocity in the shock-attached frame squared, $c^2 - |\boldsymbol{u} - \boldsymbol{D}|^2$. The sonic locus, which is denoted by the thick black curve, is where the magnitude of velocity in the shock-attached frame equals the local sound speed and roughtly indicates the domain of dependence for the flow affecting the detonation front propagation [31]. Behind this curve, small acoustic disturbances propagate away from the shock. Since the sonic locus curve intersects the shock front at the material interface, the detonation is considered unconfined as desired.

In addition to the unconfined nature of the HE, it is also useful to establish that the detonation relaxes to a steadily traveling wave by examining the phase speed of the detonation. Figure 8 shows the phase speed at the centerline, material interface, and mid-span between these two points at a resolution of $\Delta\xi = \Delta\eta = 1/8\ mm$. As the material interface follows a prescribed motion, the phase speed slows from D_{CJ} first at the edge which is followed by a slowing of the mid-span speed and finally, the centerline speed. At late time, all phase speeds relax to the same value of $D_0 \approx 6.905\ mm/\mu s$; thus indicating detonation that has relaxed to a steadily traveling wave.

For the comparison with shock-capturing, the previously run simulations of [2] are utilized. These simulations used a nominally second-order, min-

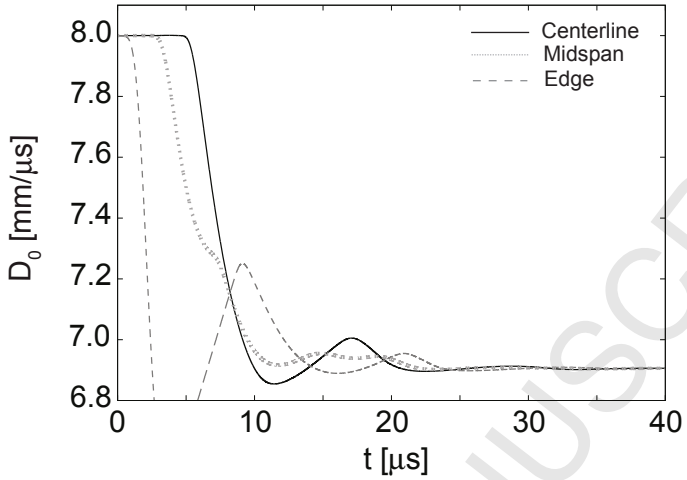

Figure 8
The detonation phase speed in a symmetric 48 mm thick slab for a PF-CAE HE at the centerline (black solid curve), the material interface (black dashed curve), and at mid-span (light gray dotted curve) at a resolution of 1/8 mm.

mod spatial scheme in conjugation with the Ghost Fluid Method of [32] to treat the multi-material interaction of the HE with a highly compressible confiner ($\rho_{0_c} = 2\ mg/mm^3$ and $\gamma = 1.4$). Note that the results presented in [2] used an early variant of ENO which results in quantitative differences than those presented here, but they are both converging qualitatively in the same fashion. Each shock-capturing simulation was run for 100 μs and the phase speeds shown in Fig. 9 and table 5 are calculated as an average over the full domain width and the final four half-thickness of the domain (96 mm) . In the case of shock-fitting, the phase speeds are averaged over the final 10 μs of the simulation.

Figure 9 compares the steady detonation phase speed for shock-fitting (black curve) with that of shock-capturing (gray curve) at several resolutions. It is clear that the shock-capturing technique is much less accurate than shock-fitting at coarse resolutions. In fact at resolution of 1/2 mm, capturing predicts $D_0 = 6.693\ mm/\mu s$ versus 6.904 $mm/\mu s$ at a resolution of 1/128 mm. Whereas, using shock-fitting at a resolution of 1/2 mm yields $D_0 = 6.897\ mm/\mu s$ which is within 0.2% of the extrapolated infinite resolution velocity of $6.9074 \pm 0.0004\ mm/\mu s$. Moreover, this means that for a user-specified error tolerance, shock-fitting needs less resolution than the capturing method, saving much computational time.

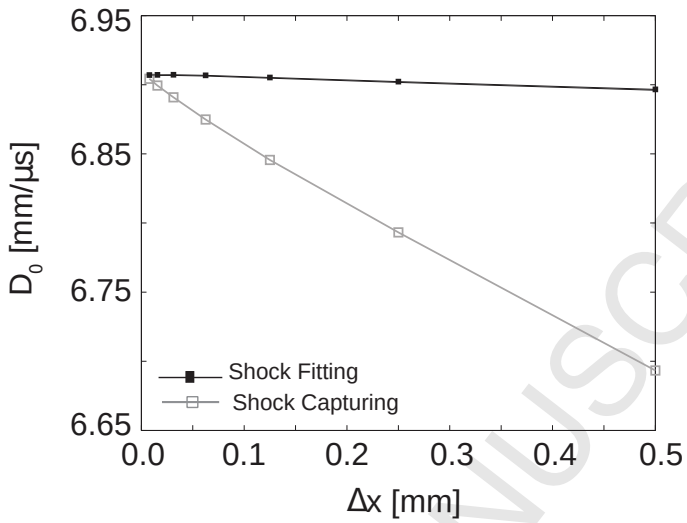

Figure 9
Convergence study of the steady detonation phase speed for a symmetric 48 mm wide slab for a PF-CAE HE comparing shock-capturing (gray curve) and shock-fitting (black curve).

Table 5 lists the averaged values shown in Fig. 9; in addition it shows a simple extrapolation to an infinite resolution. For shock-capturing this is 6.909 ± 0.005 $mm/\mu s$, which is produced using the finest two resolutions and assuming first-order convergence; this is probably better than can be expected due to the smearing of the shock. In the case of shock-fitting, the finer resolutions likely begin to show the buildup of error due to the use of the lower-order approximations utilized near the material interface; thus, the infinite resolution approximation is made using resolutions of $1/16$ mm and $1/32$ mm. Furthermore, the shock-fitting case prediction of 6.9074 ± 0.0004 $mm/\mu s$ is within the error predicted by the shock-capturing scheme. This indicates that it is likely that both methods are converging towards the same steady detonation phase speed. For a case where the user specifies an error tolerance of 0.01 $mm/\mu s$, shock-fitting is more than 4000 times more efficient.

5.2. WSD EOS Slabs and Axisymmetric Rate-Sticks

The second application of the shock-fitting method is predicting the thickness-effect curve for PBX 9501 utilizing a more realistic and complex EOS given by the WSD model. The parameters for this model are taken

Table 5
Steady Phase Speed Convergence

Resolution	Shock-Capturing	Shock-Fitting
(mm)	D_0 $(mm/\mu s)$	D_0 $(mm/\mu s)$
1/2	6.6933	6.8967
1/4	6.7932	6.9022
1/8	6.8456	6.9053
1/16	6.8749	6.9068
1/32	6.8909	6.9072
1/64	6.8994	6.9072
1/128	6.9043	6.9070
$1/\infty$	6.909 ± 0.005	6.9074 ± 0.0004

from [11] and are given by $\rho_0 = 1.844\ mg/mm^3$, $p_0 = 0\ GPa$, $k = 110\ 1/\mu s$, $\nu = 0.93$, $N_p = 3.5$, $E = 0\ mm^2/\mu s^2$, and $B = p_{CJ} = 36.3\ GPa$. At this ambient density $D_{CJ} \approx 8.860\ mm/\mu s$ which is moderately higher than that observed in experiments for PBX 9501 of $D_{CJ} \approx 8.800\ mm/\mu s$. This mismatch in D_{CJ} is partly due to using a higher than usually measured ambient density ($\rho_0 = 1.836\ mg/mm^3$) . However, even correcting for the difference in ambient density, the D_{CJ} from experimental correlation would only be $\sim 8.840\ mm/\mu s$. The choice of these parameters yields a moderately stiff reaction with a CJ half reaction zone length of $\sim 7\ \mu m$ and full reaction zone of $\sim 500\ \mu m$.

An additional complication of realistic EOSs, like those used in the WSD model, is that typical detonations propagate at finite Mach numbers usually in the range of 3−5. This fact has two ramifications worth pointing out. First, the maximum streamline deflection for a single oblique shock results in a post-shock subsonic flow. Thus to replicate the unconfined nature rate sticks, the streamline must be deflected past this point by introducing a Prandtl-Meyer expansion fan. Second, the maximum streamline deflection for a single oblique shock will also become a function (although a weak one [11]) of the detonation phase velocity, which is part of the solution sought. Although the streamline deflection angle is explicitly a function of the phase speed, near the maximum sonic angle this correlation is a weak relationship for detonating phase speeds. Moreover, the maximum deflection angle occurs at higher phase speeds [26]. For this reason, the deflection angle is evaluated at

D_{CJ}, since for finite sized charges, the propagation speed is expected to be below this speed. From the shock polar analysis of this model, the maximum streamline deflection angle at D_{CJ} is $\sim 12.1°$. This corresponds to final slope of the material interface of $m \approx 0.215$. Since the reaction rate is faster, the time constant utilized for the motion of the material interface is $\tau_c = 0.5\ \mu s$.

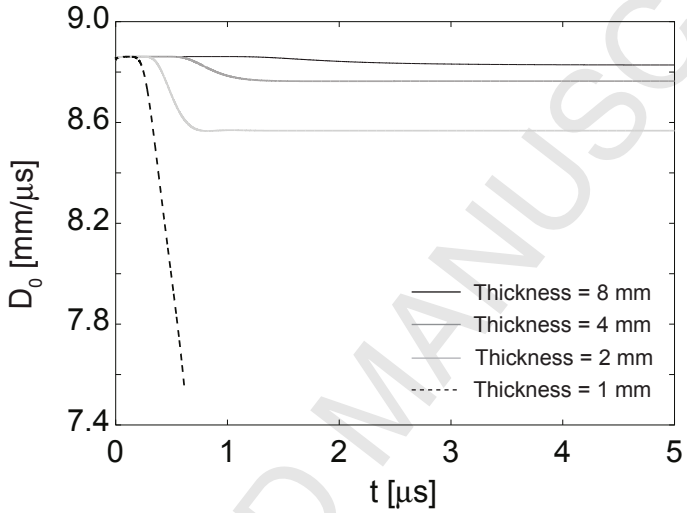

Figure 10
Centerline phase speed versus time for four slab thickness using the WSD model from [11].

Figure 10 is a plot of the centerline phase speed versus time for several slab thicknesses utilizing a resolution of 5 μm; such a fine resolution is necessary to begin resolving the reaction zone. The phase speed of the 8 mm wide slab (black solid curve) is only slightly retarded by the material interface deflection and relaxes to $D_0 = 8.843\ mm/\mu s$. As the thickness is reduced further, the steady phase speed is also reduced ($w = 4\ mm$, $D_0 = 8.764\ mm/\mu s$ - dark gray line and $w = 2\ mm$, $D_0 = 8.568\ mm/\mu s$ - light gray line); however, below a critical thickness, the detonation fails. An example below this critical threshold is $w = 1\ mm$ which is shown by the black dashed line.

By examining several more slab thickness, a thickness-effect curve is produced, which is shown in Fig. 11(a). The dashed gray curve representing a curve fit through the open squares which are the points simulated. In addition, the experimental fit/data from [33] is represented by the black curve with filled squares. This experimental thickness curve for the phase speed is

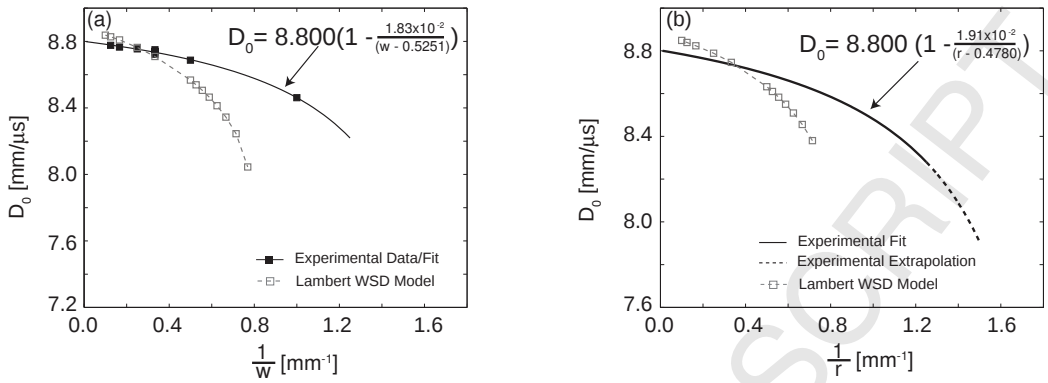

Figure 11
(a) Thickness effect curve for PBX 9501 utilizing WSD [11] predicted by shock-fitting and experimental data from [33]and (b) diameter effect curve for PBX 9501 utilizing WSD [11] predicted by shock-fitting and experimental fit from [33] and [34].

$D_0 = 8.800\,[1 - (1.83 \times 10^{-2})\,/\,(w - 0.5251)]$. The model strongly over predicts the effects of slab thickness on D_0; at wider slabs it predicts higher phase speeds than observed as expected due to the high value of D_{CJ}. However, the model also predicts detonation failure at a slab width of $\sim 1.2\ mm$, which is larger than that observed in experiments. This mis-prediction by the model is due to the model being calibrated to replicate the Shock-to-Detonation Transition (SDT). While examining the predicted behavior at finer resolutions, it is found that the model begins to develop oscillations; this suggests an instability under resolution similar to that predicted in [14].

In addition, using this same methodology with the axisymmetric source terms, a diameter effect curve can be created by plotting the phase speed versus radius of the rate stick. Figure 11(b) shows the predicted diameter curve for the PBX 9501 model (dashed gray curve with open squares) utilizing a resolution of 5 μm. The experimental fit, which is indicated by the solid black curve, is taken from [33], $D_0 = 8.800\,[1 - (1.91 \times 10^{-2})\,/\,(r - 0.4780)]$, and is in good agreement with the fit given by [34]. The dashed part of the curve is conjecture by [34] based on the similarity between PBX 9501 and PBX 9404, as both are high percentage HMX based HEs. In a similar manner to that of the thickness effect curve, the model over predicts the phase speed at larger diameters and under predicts it at the smaller diameters. Furthermore, the failure diameter is also mis-predicted dramatically.

Table 6
Calibration Experiments

Radius	Ambient Density	Observed Phase Speed	Predicted Phase Speed
$r\ (mm)$	$\rho_0\ (mg/mm^3)$	$D_0\ (mm/\mu s)$	$D_0\ (mm/\mu s)$
0.790	1.832	8.2590	8.2590
1.005	1.832	8.4870	8.4793
1.415	1.832	8.6120	8.6212
2.505	1.832	8.7220	8.7243

5.3. Reaction Model Calibration

The last application of the method examined in this paper is a calibration to the detonation regime of the reaction parameters of the WSD model for PBX 9501. More specifically, after correcting D_{CJ} by adjusting the heat release of reactants in the WSD model ($q = 5.69$), the variables used in the calibration are a, ν, and N_p. The calibration is automated using the downhill simplex method from [35] and utilized four rate-stick experiments which are shown in table 6. After 35 downhill simplex iterations (272 total rate stick simulations) and optimized set of parameters were found: $a = 1.9155$, $\nu = 0.9562$, and $N_p = 3.3898$. The diameter-effect curve using the calibrated model is shown by the light gray dashed curve with open squares in Fig. 12(b). The calibrated diameter-effect curve lies directly on top of that developed from experiments (shown by the black solid curve) as expected. Figure 12(a) shows the predicted thickness-effect curve (shown by the gray dashed line with open squares) using the calibrated reaction model. This curve is in much closer agreement with that developed from experiments by [33] than the model developed from the SDT data; however, it still slightly under predicts the phase speed of the detonation in narrower slabs. The discrepancies between the prediction for rate stick and slab type geometries is also present in detonation shock dynamics [33, Figure 9].

It should be noted that while the newly re-calibrated model preforms well for multi-dimensional detonation propagation, it is unlikely that this will preform well at predicting SDT. This is due to the simple reaction rate with only three parameters to adjust. The re-calibration of the reaction parameters to the detonation regime is meant to demonstrate the utility of the presented algorithm. Further work remains to be performed to fully calibrate reactive flow models in greater detail.

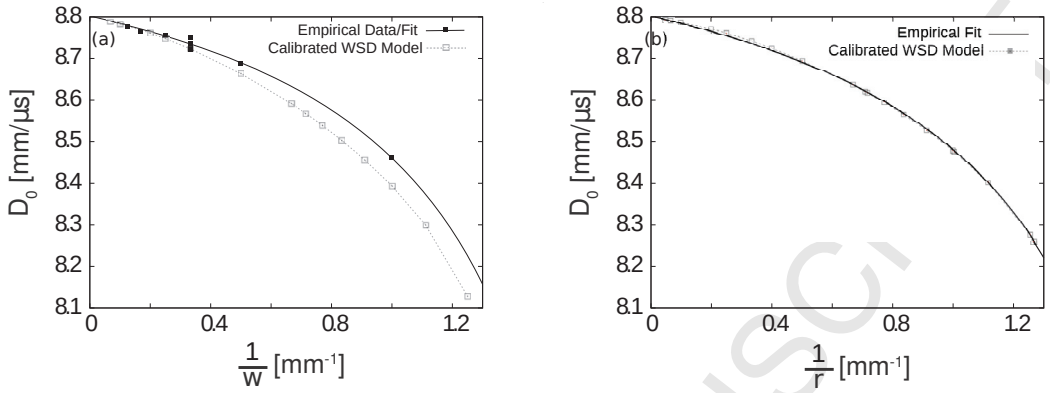

Figure 12
(a) Thickness effect curve and (b) diameter effect curve for PBX 9501 predicted by shock-fitting utilizing the calibrated reaction model versus the experimental fits from [33].

6. Conclusions

The present shock and material interface fitting algorithm is a highly accurate strategy for examining multi-dimensional shock and detonation flows even with moderately coarse grids. In fact by fitting the interfaces to computational boundaries, the discontinuities and the associated smearing effects from shock-capturing are removed. Thus, the method also offers the possibility of high rates of convergence as demonstrated by several verification tests, where fifth-order convergence rates of solutions were demonstrated. Moreover, the highly-accurate nature of the algorithm is more clear when compared with results produced using capturing. For the case of the PF-CAE EOS HE application, there is a computational savings of 4096 over capturing for an error on the $\mathcal{O}(10\ m/s)$, which is a similar uncertainity to that observed in experiments on HEs. This savings is realized through the reduction in necessary resolution in each direction as well as the corresponding larger time-step. The removal of the ambiguity of the shock state could play an even greater role in other reactive flow models which utilize the shock state during the evaluation of the reaction.

Utilizing the present fitting algorithm, a thickness effect curve was produced. It is found that the published parameters for the WSD reactive flow model for PBX 9501 predict a significantly steeper curve than obtained from experimental data. Likewise, the predicted diameter effect curve also

shows a significantly stiffer effect with respect to charge size than that observed in experiments. Moreover, the utility of the fitting method is demonstrated through the re-calibration of the reactive parameters for the detonation regime. This re-calibration was automated using a multi-variable downhill simplex method in conjunction with the shock-fitting algorithm. After this calibration, the model diameter effect curve reproduces that observed from experiments. Furthermore, the thickness effect curve produced using the re-calibrated parameters closely mimics that of the experimental data.

The highly accurate nature of the fitting algorithm, when employed appropriately, gives rise to further opportunities for study, particularly in HE modeling. This includes work with more complex geometry constraints, *e. g.* cone type tests [36], and multi-layered problems [37], *e. g.* HE surrounded by a confiner [30], both of which can lead multiple traveling shocks. In order to deal with such geometries, the current algorithm likely must be modified to handle the triple shock interaction and overtaking shocks to add stability as most fitting algorithms are susceptible to failure at these points due the high-order stencils utilized in the spatial derivative calculations. This adds additional complexity to the presented algorithm and thus, it is left for a future paper.

Acknowledgments

The authors would like to thank B. L. Wescott for sharing his wide-ranging EOS code. The authors are also grateful to J. B. Bdzil for his thoughts throughout the development of this manuscript. Likewise, the authors are appreciative of cross-verfications performed by C. Chiquete, as well as the experimental data for PBX 9501 shared by S. I. Jackson and M. Short. This study was performed under the auspices of the US Department of Energy and the National Nuclear Security Administration.

References

[1] B. Dobratz, LLNL explosives handbook: Properties of chemical explosives and explosive simulants, Tech. Rep. UCRL-52997, Lawrence Livermore National Laboratory, 1981.

[2] T. D. Aslam, J. B. Bdzil, L. G. Hill, Extension to DSD Theory: Analysis of PBX 9502 Rate Stick Data, Eleventh Symposium (Intl) on Detonation (1998) 21–29.

[3] B. L. Wescott, D. S. Stewart, W. C. Davis, Equation of State and Reaction Rate for Condensed-Phase Explosives, Journal of Applied Physics 98 (5) (2005) 053514.

[4] R. Menikoff, M. S. Shaw, The SURF Model and the Curvature Effect for PBX 9502, Combustion Theory and Modelling 16 (6) (2012) 1140–1169.

[5] C. Handley, H. J. Lacy, B. D. Lambourn, N. Whitworth, H. R. James, CREST Models for PBX 9501 and PBX 9502, Fifteenth Symposium (Intl) on Detonation (2014) 82–92.

[6] X. Zhong, High-Order Finite-Difference Schemes for Numerical Simulation of Hypersonic Boundary-Layer Transition, Journal of Computational Physics 144 (2) (1998) 662–709.

[7] D. A. Kopriva, Shock-fitted Multidomain Solution of Supersonic Flows, Computer Methods in Applied Mechanics and Engineering 175 (3) (1999) 383–394.

[8] G. P. Brooks, J. M. Powers, Standardized Pseudospectral Formulation of the Inviscid Supsersonic Blunt Body Problem, Journal of Computational Physics 197 (1) (2004) 58–85.

[9] M. Najafi, K. Hejranfar, V. Esfahanian, Application of a Shock-Fitted Spectral Collocation Method for Computing Transient High-Speed Inviscid Flows Over a Blunt Nose, Journal of Computational Physics 257 (2014) 954–980.

[10] A. K. Henrick, T. D. Aslam, J. M. Powers, Simulations of Pulsating One-Dimensional Detonations with True Fifth Order Accuracy, Journal of Computational Physics 213 (1) (2006) 311–329.

[11] D. E. Lambert, D. S. Stewart, S. Yoo, B. L. Wescott, Experimental Validation of Detonation Shock Dynamics in Condensed Explosives, Journal of Fluid Mechanics 546 (2006) 227–253.

[12] M. Vinokur, Conservation of Gas Dynamics in Curvilinear Coordinate Systems, Journal of Computational Physics 14 (2) (1974) 105–125.

[13] A. K. Henrick, Shock-Fitted Numerical Solutions of One-and Two-Dimensional Detonation, Ph.D. thesis, University of Notre Dame, 2008.

[14] M. Short, I. I. Anguelova, T. D. Aslam, J. B. Bdzil, A. K. Henrick, G. J. Sharpe, Stability of Detonations for an Idealized Condensed-Phase Model, Journal of Fluid Mechanics 595 (2008) 45–82.

[15] A. K. Henrick, T. D. Aslam, J. M. Powers, Mapped Weighted Essentially Non-Oscillatory Schemes: Achieving Optimal Order Near Critical Points, Journal of Computational Physics 207 (2) (2005) 542–567.

[16] S. Xu, T. D. Aslam, D. S. Stewart, High Resolution Numerical Simulation of Ideal and Non-Ideal Compressible Reacting Flows with Embedded Internal Boundaries, Combustion Theory and Modelling 1 (1997) 113–142.

[17] C.-W. Shu, S. Osher, Efficient Implementation of Essentially Non-Oscillatory Shock-Capturing Schemes, Journal of Computational Physics 77 (2) (1988) 439–471.

[18] G.-S. Jiang, C.-W. Shu, Efficient Implementation of Weighted ENO Schemes, Journal of Computational Physics 126 (2) (1996) 202–228.

[19] C. B. Macdonald, Constructing High-Order Runge-Kutta Methods with Embedded Strong-Stability-Preserving Pairs, Master's thesis, Simon Fraser University, 2003.

[20] L. I. Sedov, Propagation of Strong Shock Waves, Journal of Applied Mathematics and Mechanics 10 (1946) 241–250.

[21] G. I. Taylor, The Formation of a Blast Wave by a Very Intense Explosion, Tech. Rep. Report RC-210, Civil Defense Research Committee, 1941.

[22] J. von Neumann, Shock Waves Started by an Infinitesimally Short Detonation of Given (Positive and Finite) Energy, Tech. Rep. Report AM-9, National Defense Research Council - Division B, 1941.

[23] H. I. Lee, D. S. Stewart, Calculation of Linear Detonation Instability: One-Dimensional Instability of Plane Detonation, Journal of Fluid Mechanics 216 (1990) 103–132.

[24] A. Busemann, Drücke auf kegelförmige Spitzen bei Bewegung mit Überschallgeschwindigkeit., ZAMM-Journal of Applied Mathematics and Mechanics/Zeitschrift für Angewandte Mathematik und Mechanik 9 (6) (1929) 496–498.

[25] G. I. Taylor, J. W. Maccoll, The Air Pressure on a Cone Moving at High Speeds, Proceedings of the Royal Society of London. Series A: Mathematical, Physical and Engineering Sciences 139 (838) (1933) 278–311.

[26] J. D. Anderson, Modern Compressible Flow: with Historical Perspective, vol. 12, McGraw-Hill New York, 1990.

[27] M. V. Dyke, An Album of Fluid Motion, Parabolic Press, 1982.

[28] T. D. Aslam, J. B. Bdzil, Numerical and Theoretical Investigations on Detonation-Inert Confinement Interactions, Twelfth Symposium (Intl) on Detonation (2002) 483–488.

[29] T. D. Aslam, J. B. Bdzil, Theoretical Investigations on Detonation-Inert Confinement Interactions, Thirteenth Symposium (Intl) on Detonation (2006) 761–769.

[30] L. G. Hill, T. D. Aslam, The Detonation Confinement Effect: Theory, Observations, and Experiments, Fifteenth Symposium (Intl) on Detonation (2014) 504–513.

[31] J. B. Bdzil, Perturbation Methods Applied to Problems in Detonation Physics, Sixth Symposium (Intl) on Detonation (1976) 352–370.

[32] R. P. Fedkiw, T. D. Aslam, B. Merriman, S. Osher, A Non-Oscillatory Eulerian Approach to Interfaces in Multimaterial Flows (The Ghost Fluid Method), Journal of Computational Physics 152 (2) (1999) 457–492.

[33] S. I. Jackson, M. Short, Scaling of Detonation Velocity in Cylinder and Slab Geometries for Ideal, Insensitive and Non-Ideal Explosives, Journal of Fluid Mechanics 773 (2015) 224–266.

[34] A. W. Campbell, R. Engelke, Diameter Effect in High-Density Heterogeneous Explosives, Sixth Symposium (Intl) on Detonation .

[35] W. H. Press, Numerical Recipes 3rd Edition: The Art of Scientific Computing, Cambridge University Press, 2007.

[36] T. R. Salyer, L. G. Hill, The Dynamics of Detonation Failure in Conical PBX 9502 Charges, Thirteenth Symposium (Intl) on Detonation (2006) 24–34.

[37] E. K. Anderson, T. D. Aslam, S. I. Jackson, Transverse Initiation of an Insensitive Explosive in a Layered Slab Geometry: Front Shapes and Post-Shock Flow Measurements, Combustion and Flame 161 (7) (2014) 1944–1954.

[38] G. B. Whitham, Linear and Nonlinear Waves, chap. 6, John Wiley & Sons, 192–196, 2011.

Appendix A. Derivatives of Jacobian

In this section the partial derivatives of the Jacobian are developed. An illustrative example is the derivative with respect to time of the Jacobian, which is given by

$$\frac{\partial J}{\partial t} = \frac{\partial}{\partial t}\left(\frac{\partial \xi}{\partial \chi}\frac{\partial \eta}{\partial z} - \frac{\partial \xi}{\partial z}\frac{\partial \eta}{\partial \chi}\right). \tag{A.1}$$

Now applying the product rule, this can be written as

$$\frac{\partial J}{\partial t} = \frac{\partial}{\partial t}\left(\frac{\partial \xi}{\partial \chi}\right)\frac{\partial \eta}{\partial z} + \frac{\partial}{\partial t}\left(\frac{\partial \eta}{\partial z}\right)\frac{\partial \xi}{\partial \chi} - \frac{\partial}{\partial t}\left(\frac{\partial \xi}{\partial z}\right)\frac{\partial \eta}{\partial \chi} - \frac{\partial}{\partial t}\left(\frac{\partial \eta}{\partial \chi}\right)\frac{\partial \xi}{\partial z}. \tag{A.2}$$

Since χ, z, and t are independent variables, their derivatives can be interchanged through the commutative property,

$$\frac{\partial J}{\partial t} = \frac{\partial}{\partial \chi}\left(\frac{\partial \xi}{\partial t}\right)\frac{\partial \eta}{\partial z} + \frac{\partial}{\partial z}\left(\frac{\partial \eta}{\partial t}\right)\frac{\partial \xi}{\partial \chi} - \frac{\partial}{\partial z}\left(\frac{\partial \xi}{\partial t}\right)\frac{\partial \eta}{\partial \chi} - \frac{\partial}{\partial \chi}\left(\frac{\partial \eta}{\partial t}\right)\frac{\partial \xi}{\partial z}. \tag{A.3}$$

Then, utilizing the chain rule to expand the χ and z derivatives,

$$\frac{\partial J}{\partial t} = \left[\frac{\partial \xi}{\partial \chi}\frac{\partial}{\partial \xi}\left(\frac{\partial \xi}{\partial t}\right) + \frac{\partial \eta}{\partial \chi}\frac{\partial}{\partial \eta}\left(\frac{\partial \xi}{\partial t}\right)\right]\frac{\partial \eta}{\partial z}$$

$$+\left[\frac{\partial\xi}{\partial z}\frac{\partial}{\partial\xi}\left(\frac{\partial\eta}{\partial t}\right)+\frac{\partial\eta}{\partial z}\frac{\partial}{\partial\eta}\left(\frac{\partial\eta}{\partial t}\right)\right]\frac{\partial\xi}{\partial\chi}$$
$$-\left[\frac{\partial\xi}{\partial z}\frac{\partial}{\partial\xi}\left(\frac{\partial\xi}{\partial t}\right)+\frac{\partial\eta}{\partial z}\frac{\partial}{\partial\eta}\left(\frac{\partial\xi}{\partial t}\right)\right]\frac{\partial\eta}{\partial\chi}$$
$$-\left[\frac{\partial\xi}{\partial\chi}\frac{\partial}{\partial\xi}\left(\frac{\partial\eta}{\partial t}\right)+\frac{\partial\eta}{\partial\chi}\frac{\partial}{\partial\eta}\left(\frac{\partial\eta}{\partial t}\right)\right]\frac{\partial\xi}{\partial z}. \tag{A.4}$$

Lastly by rearranging terms, the derivative of the Jacobian with respect to t can be written as

$$\frac{\partial J}{\partial t}=\left[\frac{\partial}{\partial\xi}\left(\frac{\partial\xi}{\partial t}\right)+\frac{\partial}{\partial\eta}\left(\frac{\partial\xi}{\partial t}\right)\right]J. \tag{A.5}$$

This procedure can likewise be performed for both the χ and z derivatives of the Jacobian, such that

$$\frac{\partial J}{\partial\chi}=\left[\frac{\partial}{\partial\xi}\left(\frac{\partial\xi}{\partial\chi}\right)+\frac{\partial}{\partial\eta}\left(\frac{\partial\xi}{\partial\chi}\right)\right]J, \tag{A.6}$$
$$\frac{\partial J}{\partial z}=\left[\frac{\partial}{\partial\xi}\left(\frac{\partial\xi}{\partial z}\right)+\frac{\partial}{\partial\eta}\left(\frac{\partial\xi}{\partial z}\right)\right]J. \tag{A.7}$$

Therefore, the derivatives of the determinant of the metric tensor $\left(\sqrt{g}\right)$ can be written in terms of the Jacobian derivatives using the chain rule,

$$\frac{\partial}{\partial t}\left(\sqrt{g}\right)=\frac{\partial}{\partial t}\left(J^{-1}\right)=-\frac{1}{J^2}\frac{\partial J}{\partial t}=-\frac{1}{J}\left[\frac{\partial}{\partial\xi}\left(\frac{\partial\xi}{\partial t}\right)+\frac{\partial}{\partial\eta}\left(\frac{\partial\xi}{\partial t}\right)\right]$$
$$=-\left[\frac{\partial}{\partial\xi}\left(\frac{\partial\xi}{\partial t}\right)+\frac{\partial}{\partial\eta}\left(\frac{\partial\xi}{\partial t}\right)\right]\sqrt{g}, \tag{A.8}$$
$$\frac{\partial}{\partial\chi}\left(\sqrt{g}\right)=-\left[\frac{\partial}{\partial\xi}\left(\frac{\partial\xi}{\partial\chi}\right)+\frac{\partial}{\partial\eta}\left(\frac{\partial\xi}{\partial\chi}\right)\right]\sqrt{g}, \tag{A.9}$$
$$\frac{\partial}{\partial z}\left(\sqrt{g}\right)=-\left[\frac{\partial}{\partial\xi}\left(\frac{\partial\xi}{\partial z}\right)+\frac{\partial}{\partial\eta}\left(\frac{\partial\xi}{\partial z}\right)\right]\sqrt{g}. \tag{A.10}$$

Appendix B. Sedov-Taylor Blast Waves

The fluid flow solution of an intense explosion caused by the deposition of a large amount of energy at a localized point is developed in this section following the work of [38, Chap. 6]. The intense explosion in a PF-CAE yields

axisymmetric flow in the strong shock limit. For fluid at with an ambient density of ρ_o and ambient pressure of p_o, this limit yields $p_o/\left(\rho_o D_N\right) \approx 0$ where D_N is the normal shock speed. Diffusive effects and body forces are negligible behind the leading shock which results in isentropic flow inside the blast radius, which is a function of time. Utilizing the definition of entropy for a PF-CAE, $s = \ln\left(p/\rho^\gamma\right)$, and the definition of the frozen sound speed squared, $a^2 = \gamma p/\rho$, the governing equations of the flow from blast origin to the shock front can be written as

$$\frac{\partial \rho}{\partial t} + x^n \frac{\partial}{\partial x}\left(x^n \rho u_x\right) = 0, \tag{B.1}$$

$$\frac{\partial}{\partial t}\left(\rho u_x\right) + x^n \frac{\partial}{\partial x}\left(x^n \rho u_x^2\right) + \frac{\partial p}{\partial x} = 0, \tag{B.2}$$

$$\frac{ds}{dt} = \frac{\partial}{\partial t}\left(\ln a^2\right) + u_x \frac{\partial}{\partial x}\left(\ln a^2\right) - (\gamma - 1)\left(\frac{\partial}{\partial t}\left(\ln \rho\right) + u_x \frac{\partial}{\partial x}\left(\ln \rho\right)\right) = 0, \tag{B.3}$$

where γ is the adiabatic exponent or equivalently, for a calorically perfect gas, the ratio of specific heats, x the spatial coordinate, u_x the velocity in the direction of the flow, and the parameter n determines the geometry of the axisymmetric flow :

$$n = \begin{cases} 0 & \text{planar geometry} \\ 1 & \text{cylindrical geometry} \\ 2 & \text{spherical geometry} \end{cases} \tag{B.4}$$

In addition to the flow behind the shock, the shock state must be determined. This accomplished using the Rankine-Huginot jump conditions; in the strong shock limit, the shock state is given by

$$\rho\left(\mathsf{R}\left(t\right)\right) = \frac{(\gamma+1)}{(\gamma-1)}\rho_o, \tag{B.5}$$

$$u_x\left(\mathsf{R}\left(t\right)\right) = \frac{2}{(\gamma+1)} D_N, \tag{B.6}$$

$$p\left(\mathsf{R}\left(t\right)\right) = \frac{2}{(\gamma+1)}\rho_o D_N^2, \tag{B.7}$$

where D_N is a function of time.

In the strong shock limit, the particle velocities and pressures behind the shock are much larger than ambient acoustic speed and the initial pressure, respectively. Therefore, there are only two dimensional parameters that play an important role in determining the flow behavior, ρ_o and E. These two parameters can be combined in a single way which is independent of mass; thus, the blast radius, $\mathsf{R}(t)$, must take the functional form

$$\mathsf{R}(t) = c_1 \left(\frac{\mathsf{E}}{\rho_o}\right)^{\frac{1}{(n+3)}} t^{\frac{2}{(n+3)}}, \tag{B.8}$$

where c_1 is a dimensionless constant. Furthermore, the speed at which the shock location changes is given by

$$\frac{d\mathsf{R}}{dt} = D_N = c_1 \left(\frac{\mathsf{E}}{\rho_o}\right)^{\frac{1}{(n+3)}} \frac{2}{(n+3)} t^{\frac{(n-1)}{(n+3)}} = \frac{2}{(n+3)\,t}\mathsf{R}(t). \tag{B.9}$$

It then follows that up to an undetermined constant, c_1, that shock state and its motions are known :

$$\mathsf{R}(t) = c_1 \left(\frac{\mathsf{E}}{\rho_o}\right)^{\left(\frac{1}{m}\right)} t^{\left(\frac{2}{m}\right)}, \tag{B.10}$$

$$D_N = \frac{2}{mt}\mathsf{R}(t), \tag{B.11}$$

$$\rho(\mathsf{R}(t)) = \frac{(\gamma+1)}{(\gamma-1)}\rho_o, \tag{B.12}$$

$$u_x(\mathsf{R}(t)) = \frac{4}{(\gamma+1)\,mt}\mathsf{R}(t), \tag{B.13}$$

$$p(\mathsf{R}(t)) = \frac{8}{(\gamma+1)\,m^2t^2}\rho_o\mathsf{R}(t)^2, \tag{B.14}$$

$$a^2(\mathsf{R}(t)) = \frac{8\gamma(\gamma-1)}{(\gamma+1)^2\,m^2t^2}\mathsf{R}(t)^2, \tag{B.15}$$

where $m = n+3$ is used for ease of notation.

For a similarity solution to exist for all time, $t > 0$, then a non-dimensional variable must exist which is composed of a combination of x and t. The blast radius is a distance which is a function of time which suggests a non-dimensional variable of

$$\zeta = \frac{x}{\mathsf{R}(t)}. \tag{B.16}$$

With this choice for similarity variable, the shock is located at $\zeta = 1$ and the blast origin at $\zeta = 0$ for all time after the initial deposition. Likewise, non-dimensional functions of density, velocity, and the squared sound speed can be defined as well :

$$D(\zeta) = \frac{\rho}{\rho_o}, \tag{B.17}$$

$$U(\zeta) = \frac{a_1 u_x t}{x}, \tag{B.18}$$

$$A(\zeta) = \frac{a_2 a^2 t^2}{x^2}, \tag{B.19}$$

where a_1 and a_2 are dimensionless constants which can be used to simplify the form of the governing equations. By substituting Eqns. B.17-B.19 into Eqns. B.1-B.3, utilizing the definition of the squared sound speed and applying the derivatives of the similarity variable, $\partial\zeta/\partial t = -2\zeta/(mt)$ and $\partial\zeta/\partial x = \zeta/x$, the governing equations can be written as

$$\frac{\rho_o}{a_1 t}\left[\zeta\left(U - \frac{2a_1}{m}\right)\frac{dD}{d\zeta} + \left(\zeta\frac{dU}{d\zeta} + (n+1)U\right)D\right] = 0, \tag{B.20}$$

$$\frac{x}{a_1^2 t^2}\left[\left(U - \frac{2a_1}{m}\right)\zeta\frac{dU}{d\zeta} + (U - a_1)U\right] + \frac{x}{a_2 t^2}\frac{1}{\gamma}\left(\frac{A\zeta}{D}\frac{dD}{d\zeta} + 2A + \zeta\frac{dA}{d\zeta}\right) = 0, \tag{B.21}$$

$$\frac{1}{a_1 t}\left[\left(U - \frac{2a_1}{m}\right)\frac{\zeta}{A}\frac{dA}{d\zeta} + 2(U - a_1) + (1-\gamma)\left(U - \frac{2a_1}{m}\right)\frac{\zeta}{D}\frac{dD}{d\zeta}\right] = 0. \tag{B.22}$$

Therefore, for all time after the energy deposition and any location between the blast origin up to and including the blast front, the governing equations can be simplified further if $a_2 = a_1^2 = m^2/4$ and $\rho_o > 0$. After this simplification, the governing equation can written using prime notation as

$$\zeta(U-1)D' + \zeta DU' + (n+1)DU = 0, \tag{B.23}$$

$$\zeta(U-1)U' + \left(U - \frac{m}{2}\right)U + \frac{1}{\gamma}\left(A\zeta\frac{D'}{D} + 2A + \zeta A'\right) = 0, \tag{B.24}$$

$$\zeta(U-1)\left[\frac{A'}{A} - (\gamma-1)\frac{D'}{D}\right] + 2\left(U - \frac{m}{2}\right) = 0. \tag{B.25}$$

In addition, this transformation can be applied to obtain the conditions at the blast front

$$D(1) = \frac{\rho(\mathsf{R}(t))}{\rho_o} = \frac{(\gamma+1)}{(\gamma-1)}, \tag{B.26}$$

$$U(1) = \frac{m u_x(\mathsf{R}(t))\, t}{2\mathsf{R}(t)} = \frac{2}{(\gamma+1)}, \tag{B.27}$$

$$A(1) = \frac{m^2 a^2(\mathsf{R}(t))\, t^2}{4\mathsf{R}(t)^2} = \frac{2\gamma(\gamma-1)}{(\gamma+1)^2}; \tag{B.28}$$

thus, the ODEs given by Eqns. B.23-B.25 could be integrated from the blast front ($\zeta = 1$) towards the blast origin ($\zeta = 0$) for the non-dimensional form of the solution.

Though Eqns. B.23-B.25 can be integrated, an analytic solution is still sought. This solution is pursued using the fact that the total energy within the blast wave is conserved; no energy enters through the shock front due the strong shock propagating into a fluid that is initially quiescent. The total energy for a PF-CAE within a radius, r, is can be obtained using the integrand:

$$\begin{aligned}\mathcal{E}(r,t) &= \int_0^r \rho\left(e + \frac{u_x^2}{2}\right)\pi^l (2\hat{r})^n \,\partial\hat{r} \\ &= \int_0^r \rho\left(\frac{a^2}{\gamma(\gamma-1)} + \frac{u_x^2}{2}\right)\pi^l (2\hat{r})^n \,\partial\hat{r},\end{aligned} \tag{B.29}$$

where

$$l = \begin{cases} 0 & \text{planar geometry} \\ 1 & \text{non-planar geometry} \end{cases} \tag{B.30}$$

The motion of the boundary is balanced by the change in ρ, u_x, and a^2 time. As the blast wave can be described as a similarity solution, the total energy between two ζ locations must remain constant, and thus, the integrand must be a function of ζ alone. Furthermore, the total energy from the origin to a ζ can be written using Eqns. B.17-B.19 as

$$\begin{aligned}\mathcal{E}(\zeta) &= \frac{2^{n+2}\pi^l \rho_o}{m^2}\int_0^\zeta D\left(\frac{A}{\gamma(\gamma-1)} + \frac{U^2}{2}\right)\frac{\hat{\zeta}^{n+2}\mathsf{R}^m}{t^2}d\hat{\zeta}, \\ &= \frac{2^{n+2}\pi^l c_1^m \mathsf{E}}{m^2}\int_0^\zeta D\left(\frac{A}{\gamma(\gamma-1)} + \frac{U^2}{2}\right)\hat{\zeta}^{n+2}d\hat{\zeta}.\end{aligned} \tag{B.31}$$

Note, that this definition contains the total energy of the blast wave, E, and the unknown constant, c_1, which is necessary to obtain the physical solution from the similarity solution. By evaluating Eqn. B.31 for $\zeta = 1$, the unknown constant can be determined :

$$\mathcal{E}(\zeta = 1) = \mathsf{E} = \frac{2^{n+2}\pi^l c_1^m \mathsf{E}}{m^2} \int_0^1 D\left(\frac{A}{\gamma(\gamma-1)} + \frac{U^2}{2}\right)\hat{\zeta}^{n+2} d\hat{\zeta}; \tag{B.32}$$

therefore,

$$c_1 = \left[\frac{2^{n+2}\pi^l}{m^2} \int_0^1 D\left(\frac{A}{\gamma(\gamma-1)} + \frac{U^2}{2}\right)\hat{\zeta}^{n+2} d\hat{\zeta}\right]^{-\frac{1}{m}}. \tag{B.33}$$

Now, applying the Reynolds' transport theorem to the conservation of energy equation and utilizing the divergence theorem yields

$$\begin{aligned}\frac{d}{dt}(\mathcal{E}(\zeta)) = 0 &= \int_{S(\zeta)} \left[\rho\left(e + \frac{u^2}{2}\right)\frac{\partial r}{\partial t} - \rho u\left(e + \frac{u^2}{2} + \frac{p}{\rho}\right)\right] dS, \\ &= \int_{S(\zeta)} \left[\rho\left(\frac{a^2}{\gamma(\gamma-1)} + \frac{u^2}{2}\right)\frac{\partial}{\partial t}(\zeta \mathsf{R}) \right. \\ &\qquad \left. - \rho u\left(\frac{a^2}{(\gamma-1)} + \frac{u^2}{2}\right)\right] dS. \end{aligned} \tag{B.34}$$

For this to be the case for any ζ, the integrand is itself must be identically zero and therefore,

$$\rho\left(\frac{a^2}{\gamma(\gamma-1)} + \frac{u^2}{2}\right)\frac{\partial}{\partial t}(\zeta \mathsf{R}) = \rho u\left(\frac{a^2}{(\gamma-1)} + \frac{u^2}{2}\right). \tag{B.35}$$

Making use of Eqns. B.17-B.19, results in an algebraic constraint of

$$\begin{aligned}\left(\frac{A}{\gamma(\gamma-1)} + \frac{U^2}{2}\right)\frac{\partial}{\partial t}(\zeta \mathsf{R}) &= \frac{2xU}{mt}\left(\frac{A}{(\gamma-1)} + \frac{U^2}{2}\right), \\ \left(\frac{A}{\gamma(\gamma-1)} + \frac{U^2}{2}\right)\frac{2x}{mt} &= \frac{2xU}{mt}\left(\frac{A}{(\gamma-1)} + \frac{U^2}{2}\right), \\ A &= \frac{\gamma(\gamma-1)}{2}\frac{(U-1)}{(1-\gamma U)}U^2, \end{aligned} \tag{B.36}$$

as long as $U \neq 1/\gamma$. Notice that the conditions

$$A(U(\zeta = 1)) = A\left(U = \frac{2}{(\gamma+1)}\right) = A(\zeta = 1) = \frac{2\gamma(\gamma-1)}{(\gamma+1)^2} \tag{B.37}$$

are satisfied. Rearranging Eqn. B.23, then substituting into Eqn. B.25, and then multiplying by $d\ln\zeta/dU$ yields

$$\frac{d\ln\zeta}{dU}\left[\frac{(U-1)}{(\gamma-1)}\frac{d\ln A}{d\ln\zeta}+\frac{dU}{d\ln\zeta}+\frac{\kappa U-m}{(\gamma-1)}=0\right], \tag{B.38}$$

$$\frac{(U-1)}{(\gamma-1)}\frac{d\ln A}{dU}+\frac{(\kappa U-m)}{(\gamma-1)}\frac{d\ln\zeta}{dU}+1=0, \tag{B.39}$$

where $\kappa=\left((\gamma-1)(n+1)+2\right)$. Then, by substituting the derivative of the natural log of Eqn. B.36,

$$\frac{d\ln A}{dU}=0+\frac{1}{(U-1)}+\frac{\gamma}{(1-\gamma U)}+\frac{2}{U}, \tag{B.40}$$

into Eqn. B.39 yields

$$\begin{aligned}&\frac{(U-1)}{(\gamma-1)}\left[\frac{1}{(U-1)}+\frac{\gamma}{(1-\gamma U)}+\frac{2}{U}\right]+\frac{(\kappa U-m)}{(\gamma-1)}\frac{d\ln\zeta}{dU}+1=0,\\ &\frac{d\ln\zeta}{dU}=\frac{\gamma(U-1)}{(m-\kappa U)(1-\gamma U)}+\frac{2(U-1)}{(m-\kappa U)U}+\frac{\gamma}{(m-\kappa U)}.\end{aligned} \tag{B.41}$$

Likewise, a relationship between the nondimensional density and velocity can be obtained through a similar procedure:

$$\begin{aligned}&\frac{d\ln\zeta}{dU}\left[\frac{d\ln D}{d\ln\zeta}=\frac{-1}{(U-1)}\frac{dU}{d\ln\zeta}-\frac{(n+1)U}{(U-1)}\right],\\ &\frac{d\ln D}{dU}=\frac{-1}{(U-1)}-\frac{(n+1)}{(m-\kappa U)}\left[\frac{\gamma U}{(1-\gamma U)}+2+\frac{\gamma U}{(U-1)}\right].\end{aligned} \tag{B.42}$$

Integrating Eqns. B.41 and B.42 with respect to U results in

$$\begin{aligned}\zeta(U)=&\left[\frac{(m-\kappa U)(\gamma+1)}{(m(\gamma+1)-2\kappa)}\right]^{\beta_1}\left[\frac{\gamma+1}{1-\gamma}(1-\gamma U)\right]^{\beta_2}\\ &\left[\frac{(\gamma+1)}{2}U\right]^{-\frac{2}{m}},\end{aligned} \tag{B.43}$$

$$\begin{aligned}D(U)=&\left[\frac{\gamma+1}{\gamma-1}\right]\left[\frac{\gamma+1}{1-\gamma}(U-1)\right]^{\beta_3}\left[\frac{(\gamma+1)(m-\kappa U)}{m(\gamma+1)-2\kappa}\right]^{\beta_4}\\ &\left[\frac{\gamma+1}{1-\gamma}(1-\gamma U)\right]^{\beta_5}\end{aligned} \tag{B.44}$$

where

$$\beta_1 = \frac{\kappa - (\gamma+1)\,m}{m\kappa} + \frac{\kappa - m}{m\,(\kappa - \gamma m)}, \tag{B.45}$$

$$\beta_2 = \frac{1-\gamma}{\kappa - \gamma m}, \tag{B.46}$$

$$\beta_3 = -\left(\frac{(n+1)\,\gamma}{m-\kappa} + 1\right), \tag{B.47}$$

$$\beta_4 = -\,(n+1)\left[\frac{\kappa - (\gamma+1)\,m}{\kappa\,(m-\kappa)} - \frac{1}{\kappa - \gamma m}\right], \tag{B.48}$$

$$\beta_5 = \frac{-\,(n+1)}{\kappa - \gamma m}. \tag{B.49}$$

However, the sought solution is for $D(\zeta)$, $U(\zeta)$, and $A(\zeta)$ not $\zeta(U)$, $D(U)$, and $A(U)$ given by Eqns. B.36, B.43, and B.44. Therefore, Eqn. B.43 must be implicitly inverted for $U(\zeta)$ by an iterative process to arbitrary accuracy. To find this solution, the values of U must be bounded. One bound for this process is at $\zeta = 1$, which known to be $U(\zeta = 1) = 2\gamma(\gamma-1)/(\gamma+1)^2$, and the other bound is determined by the evaluation of $\zeta(U) = 0$. This means the lower bound is given by the maximum of three possiblities, $U = 0$, $U = 1/\gamma$, and $U = m/\kappa$ which is also less than the upper bound. Given that $\gamma > 1$, the bounds are given by

$$\frac{2}{\gamma+1} \geq U \geq \begin{cases} \frac{1}{\gamma} & \text{if } (m-4)\,\gamma < (3m-8) \\ \frac{m}{\kappa} & \text{if } m = 5 \text{ and } \gamma > 7 \end{cases} \tag{B.50}$$

Lastly, Eqn. B.33 must be rewritten in terms of U to obtain the physical solution from the similarity solution :

$$c_1 = \left[\frac{2^{n+2}\pi^l}{m^2} \int_{\frac{1}{\gamma} \text{ or } \frac{m}{\kappa}}^{\frac{2}{\gamma+1}} D\left(\frac{A}{\gamma(\gamma-1)} + \frac{\hat{U}^2}{2}\right)\zeta^{n+2}\frac{d\zeta}{d\hat{U}}d\hat{U}\right]^{-\frac{1}{m}}. \tag{B.51}$$